IDA

INSTITUTE FOR DEFENSE ANALYSES

Flash Lidar: Monte Carlo Estimates of Ballistic, Diffuse, and Noise Photons as Recorded by Linear and Geiger Detector Arrays

Roger Sullivan
John Franklin
James Heagy

March 2004

IDA Paper P-3833
Log: H 03-002191

This work was conducted under contracts DASW01 98 C 0067/ DASW01 04 C 0003, Task CRP-2075, for DARPA. The publication of this IDA document does not indicate endorsement by the Department of Defense, nor should the contents be construed as reflecting the official position of that Agency.

INSTITUTE FOR DEFENSE ANALYSES

IDA Paper P-3833

Flash Lidar: Monte Carlo Estimates of Ballistic, Diffuse, and Noise Photons as Recorded by Linear and Geiger Detector Arrays

Roger Sullivan
John Franklin
James Heagy

PREFACE

This paper was completed under an IDA Central Research Project.

CONTENTS

FIGURES

TABLES

1. INTRODUCTION

Many circumstances exist for which one may wish to identify, or at least image, a distant object (target), for example, a vehicle, when one cannot see the object clearly because of obscuration, such as fog, smoke, or haze. A useful technique for performing such imagery may be laser imaging radar, or lidar. Key advantages of lidar are (1) using short pulses, one may determine a range profile, (2) using receiving optics, one may determine azimuth and elevation resolution. Because the transmitted electromagnetic radiation is either visible or infrared, the relatively short wavelength provides a diffraction-limited angular resolution much finer than for microwave radar, for which target rotation is usually required to obtain fine cross-range resolution.

A particularly useful lidar concept is "flash lidar." A single laser pulse illuminates the entire target. Scattered light (photons) from various parts of the target is received by the lidar optics and focused onto an array of detectors. Because the target is usually quite far from the lidar, the array of detectors (called the "focal plane array," or FPA) is typically in the focal plane. A target image is thereby formed; each detector produces a single pixel. Each detector is also assumed capable of resolving the arrival time of a photon. When this arrival time is interpreted as a delay t_d relative to the arrival time of a photon from the part of the target nearest the lidar, then the depth of the pixel may be inferred as $ct_d/2$, and a 3D image, consisting of a 3D array of *voxels,* may be formed.

Some photons travel through the obscurant without scattering; these are termed "ballistic" photons and can produce an undistorted 3D image. Others are scattered but nevertheless reach the FPA; these "diffuse" photons interfere with the clarity of the target image. For given assumptions about the parameters of the lidar (including detector noise level), obscurant, and target, our model simulates a 3D target image and, for each voxel, indicates the number of detector counts due to ballistic photons, diffuse photons, and noise.

2. FLASH LIDAR

We assume a circular receive aperture (lens or mirror) of diameter D and focal length d, with an FPA consisting of $n_x \times n_y$ detectors (pixels), with center-separation (pitch) $w << d$. The single-pixel ("instantaneous") field-of-view (IFOV) is then w/d (radians) and the overall field-of-view (FOV) is $\sim n_x\ w/d$ x $n_y\ w/d$. Because the target and/or lidar platform may be moving, it is advantageous to transmit a short pulse and receive the echo pulse on all detectors in parallel. Each detector records the arrival time of photon(s), quantizing this into a series of "time bins." This concept is "flash lidar" as opposed to the more traditional scanning lidar. The plane in which the target is focused is the image plane. We assume that the target is relatively far from the lidar, and that the image plane is therefore the focal plane. We also assume that the flash lidar is not a search device, but that the target has been already located by another sensor, for example, a microwave radar or a forward-looking infrared (FLIR). The lidar is a "soda-straw" sensor, used for target recognition and identification. Figure 1 presents an overview of the flash lidar concept.

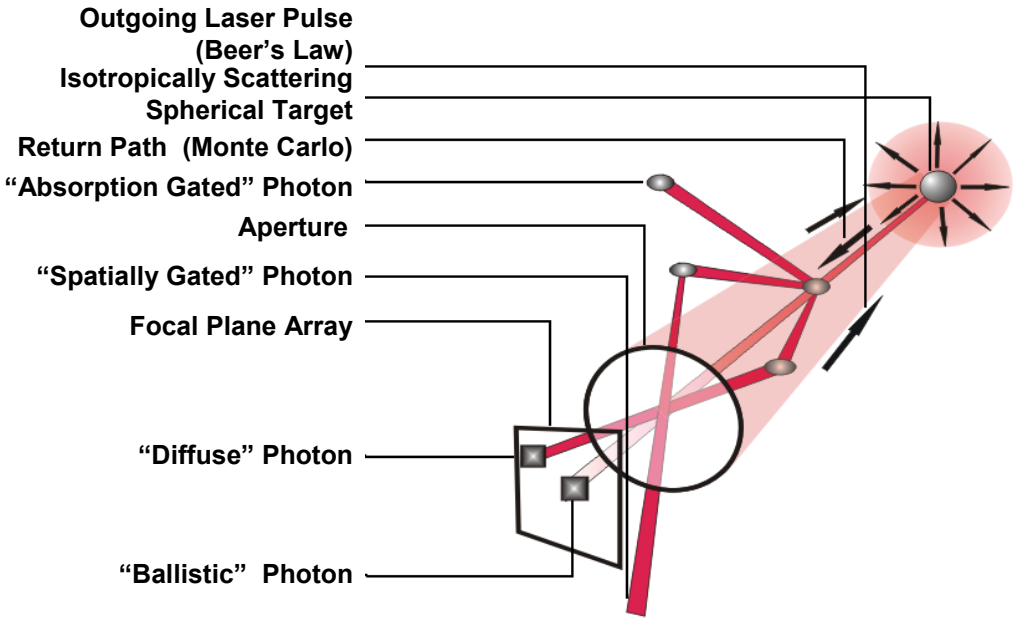

Figure 1. Flash Lidar—Overview

The lidar transmits a pulse of energy E (millijoules) and width τ (nanoseconds). The beam is assumed to be well collimated, such that, in the absence of obscurants, most of the energy strikes the target, which is at range R, and all of the target is illuminated by the beam. Scattering from the target is assumed to be isotropic (see Section 4). Scattered energy is received by the lidar optics and focused onto the FPA.

If obscurant is present (assumed for now to be homogeneous everywhere in space), then lidar energy moving a distance z through the obscurant will decay according to $\exp(-z/L)$, where z is the distance traveled, and L is the scattering length and equals the mean free path of the photon ([1], p. 259). This simple equation is known as Beer's Law ([2], Vol. 3, p. 4). The unscattered photons continue to travel in a straight line. After Wang et al. [3] we refer to these as "ballistic" photons. Each time a photon is scattered, the probability of its not being absorbed is the single-scattering albedo; the photons that are scattered but not absorbed are referred to as "diffuse" photons. (Wang et al. [3] also refer to "snake" photons as those that are scattered, but not enough to hit a different detector element. We prefer to avoid this term.) Values of $\gamma = 1/L$ for some typical obscurants and wavelengths are given in [4].

When a fog or other atmospheric obscurant has a "visibility" characterized by a particular range, then, at that range, the received intensity is two percent of the clear-air value. Thus the "visibility" = 3.912 scattering lengths [4], since $e^{-3.912} = 0.02$.

When a pulse is transmitted, the estimated number of ballistic photons received by a single detector (pixel) is then

$$N_b = \frac{E}{(hc/\lambda)} \rho \frac{\pi (D/2)^2}{4\pi R^2} \frac{1}{N_{pix}} \eta \cdot e^{-2R/L} \quad , \tag{1}$$

where λ is the photon wavelength, h is Planck's constant, c is the speed of light, hc/λ is the energy of a single photon, E is the pulse energy, R is the range to the target, L is the scattering length, D is the aperture diameter, ρ is the target reflectivity, N_{pix} is the number of pixels occupied by the target image in the FPA. η is the "overall efficiency" and includes such parameters as overlap of beam and target, optics transmission, FPA fill factor (ratio of area occupied by detectors to total FPA area), and detector quantum efficiency. We assume that $\eta = 0.1$. We assume that, by the time the first ballistic photons arrive at the FPA, the rate of arrival of received "pathback" photons (those scattered from the obscurant as the pulse travels to the target) is small compared with the rate of arrival of ballistic and diffuse photons scattered from the front (nearest point) of the target. This assumption is supported by experiments [5].

Before performing a detailed Monte Carlo calculation, it is important to compute N_b. If N_b is large, say > 1,000, then it is probably straightforward to obtain a clear image. If N_b is less than ~1, then a clear image may not be possible using a single laser pulse, though it may be possible using pulse integration and a very low-noise detector. Figure 2 shows N_b for some specific parameter values.

$h := 6.626\,10^{-34}\cdot J\cdot s \qquad c := 3\cdot 10^{8}\cdot m\cdot s^{-1}$

$\lambda := 1.54\,10^{-6}\cdot m \qquad Epulse := 40\cdot 10^{-3}\cdot J$

$D := 6\cdot cm \qquad \eta overall := 0.1 \qquad Nx := 27 \qquad Ny := 67 \qquad \rho tgt := 0.1$

$$Nph_{i,j} := \frac{Epulse}{\left(\frac{h\cdot c}{\lambda}\right)}\cdot e^{-RoverL_j}\cdot\frac{\pi\cdot\left(\frac{D}{2}\right)^2}{4\cdot\pi\cdot\left(R_i\right)^2}\cdot\frac{1}{Nx\cdot Ny}\cdot\rho tgt\cdot\eta overall \qquad NBph_{i,j} := Nph_{i,j}\cdot e^{-RoverL_j}$$

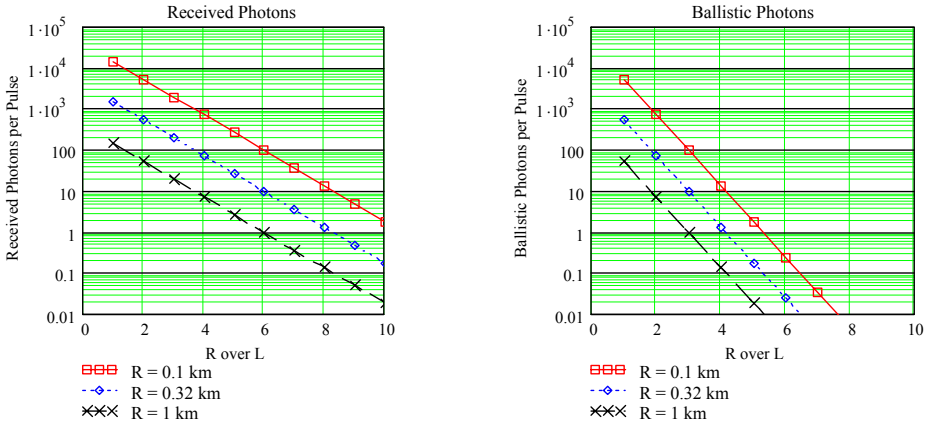

Figure 2. Estimated Number of Total and Ballistic Photons per Pixel

3. PHOTON SCATTERING

To consider the scattering of a photon, we use two spherical coordinate systems - a "lab frame," with the z-axis along the initial photon direction, and a "photon frame," whose *z* axis is along the current direction of propagation (initially, the two frames are co-aligned). At each scattering event the new direction and new photon frame is characterized by polar angle θ and azimuthal angle ϕ, measured with respect to the previous photon frame. The distribution of scattering directions is given by the *phase function* $P(\theta,\phi)$ ([6], Vol. 2, Chapter 10). We assume a simple model such that ϕ is distributed uniformly from 0 to 2π (photon polarization effects are neglected), and the distribution over θ is given by $\Phi(\theta)$ (the standard notation [6]). The normalization is as follows:

$$\begin{aligned} &P(\theta,\phi)d\theta d\phi = \Phi(\theta)\sin(\theta)d\theta d\phi \\ &\int_0^{2\pi}\int_0^{\pi} \Phi(\theta)\sin(\theta)d\theta d\phi = 4\pi \quad . \\ &\int_0^{\pi} \Phi(\theta)\sin(\theta)d\theta = 2 \end{aligned} \tag{2}$$

The actual form of Φ is given by Mie theory. Because it is complicated, a simple approximation is typically used. Many such approximations exist. We chose the Henyey-Greenstein (HG) function ([6], Vol. 2, p. 307) because it is widely used and mathematically tractable:

$$\Phi(g,\theta) = \frac{1-g^2}{\left(1+g^2-2g\cos\theta\right)^{3/2}} \ , 0 < g < 1 \quad . \tag{3}$$

The parameter g characterizes the degree of forward scattering. Isotropic scattering occurs for $g = 0$. Plots of $\Phi(g,\theta)$ are given in Figure 3. The procedure for generating a random θ according to this distribution is given in Appendix A. Approximate values of g for some obscurants are also given in [7], based on [6], Vol. 2, Chapter 10.

$$\Phi(g,\theta)=\frac{1-g^2}{\left(1+g^2-2g\cos(\theta)\right)^{3/2}}$$

g(typical, 1.54 μm)=

~0.05 – haze
~0.6 -- smoke
~0.8 – 0.9 – fog, cloud, rain

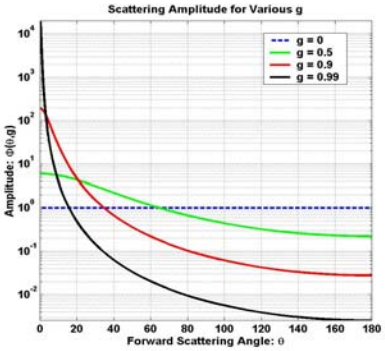

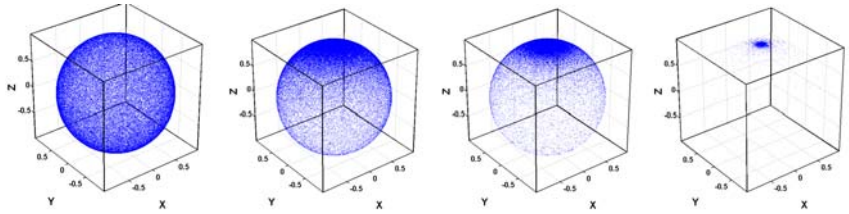

g = 0 **g = 0.3** **g = 0.6** **g = 0.9**

Figure 3. Scattering Angle Distributions

4. MONTE CARLO MODEL

The IDA Flash Lidar Monte Carlo Model works as follows. (An earlier version was described in [7].) From the lidar to the target, the intensity of the beam is computed simply by Beer's Law. We assume no absorption by the obscurant (often a good assumption [6]). The total number of photons that are scattered isotropically from the target and return to a detector in the lidar FPA is then given by

$$N_{total} = \frac{E}{(hc/\lambda)} \rho \frac{\pi (D/2)^2}{4\pi R^2} \frac{1}{N_{pix}} \eta \cdot e^{-R/L} = N_b e^{R/L} \tag{4}$$

because each photon scattered from the target eventually reaches the surface of the sphere of radius R centered at the target.

Each photon scattered from the target is modeled separately. The photon leaves the target in a specified direction ($\Theta = 0$, $\Phi = 0$ in the lab frame). The path length l between successive scattering events is selected randomly from an exponential distribution $f(l) = \frac{1}{L} e^{-l/L}$; this is carried out by choosing u from a uniform random distribution on [0,1] and computing $l = -L \ln(u)$ (see also [7]). The new scattering direction is then chosen by randomly selecting the scattering angles θ and ϕ, as described above. The transformation from lab frame is accomplished by a suitable product of rotation matrices, the exact form of which is given in Appendix C. This scattering procedure is iterated until the photon range exceeds R, at which point the model computes the exit time, values of θ,ϕ, and values of Θ,Φ. We then invoke the assumption of isotropic scattering from the target: for each photon leaving the target at 0,0 and exiting the sphere at (Θ,Φ), there is an equally likely photon leaving the target at $(\pi-\Theta,-\Phi)$ and exiting the sphere at (0,0). Therefore each modeled photon can be considered as a photon that strikes the lidar aperture. This procedure greatly decreases computation time. Computer time is also saved by terminating consideration of any photon whose travel time is greater than the time corresponding to the last time bin being recorded by the detector. The model also includes the option of assuming that the obscurant is confined to a layer between concentric spheres of radii R_1 and R_2 ($0 \le R_1 \le R_2 \le R$).

Many photons that strike the aperture still do not strike the FPA, since their incident angle is too large; these are "spatially-gated" photons—see Figure 1. For each

photon striking the aperture, whether ballistic or diffuse, the model computes the FPA detector element (n_x, n_y) that it strikes (if any), and the delay time t.

Three-dimensional plots of incident photons versus n_x (width), n_y (height), and t (depth) are produced. The time spacing Δt corresponds to the FPA time resolution; the laser pulse width is assumed to be much shorter. The 3D voxel spatial dimensions are then w x w x $c\Delta t/2$ (assuming a FPA fill factor of 1.0).

The user specifies the mean number of noise counts ("noise photons") per voxel, which depends on the type of detector being used. The number of noise counts in the voxel is then chosen randomly according to a Poisson distribution. The model considers both *linear detectors*, which record the number of incident photons plus noise counts, and *Geiger detectors,* which record "1" if the total of incident photons plus computed noise counts in the voxel exceeds unity. The model accounts for the fact that, once a Geiger detector has recorded a photon, its relatively long recovery time prevents it from detecting another photon scattered from the same laser pulse. (We assume that the pulse repetition frequency [PRF] is low enough that the detector recovers before the next pulse is received.) The model also allows for integration of a number of laser pulses. After pulse integration, the mean of the noise is subtracted. It is assumed that the sensor is well characterized, the noise is stationary, and the mean of the noise is well known.

We expect the numbers of ballistic and diffuse photons in a voxel to be Poisson-distributed (and we specifically assume the noise to be Poisson), since they all satisfy criteria described in [9]: "The Poisson distribution describes the population of events in any interval of x (e.g., space or time) whenever (a) the number of events in any interval of x is independent of that in any other non-overlapping interval; (b) in any small Δx, the probability of one event is $\lambda \Delta x$ and the probability of two or more vanishes at least as fast as $(\Delta x)^2$ as $\Delta x \rightarrow 0$; and (c) λ does not depend on x. Then [the mean] $\mu \equiv \lambda x$; $E(n) = \mu$; $\mathrm{Var}(n) = \mu$."

Table 1 presents a summary of the inputs and outputs of the Monte Carlo model.

Table 1. Summary of Monte Carlo Model Inputs and Outputs

(B = ballistic photons, D = diffuse photons, N = noise photons, Nmean = average of noise counts over FPA)

Given:

- **Pulse energy**
- **Wavelength**
- **Range (R)**
- **R_1, R_2 = inner and outer ranges of obscurant layer (target is R = 0)**
- **$(R_2 – R_1)/(L$ (L = scattering length)**
- **Henyey-Greenstein factor = g (could be generalized), scattering Albedo = a**
- **Target reflectivity (target isotropic, "Lambertian," or "specular")**
- **Aperture diameter**
- **Focal length**
- **FPA size (n_x, n_y)**
- **Pitch**
- **Overall efficiency (includes fill factor, optics, transmission, quantum efficiency)**
- **Time gate (assumed >> laser pulse width)**
- **Number of time gates**
- **Number of pulses integrated**
- **Mean of noise (assume Poisson)**
- **Detector type: linear or Geiger**

Compute:

- **B, B + D, B + D + N, B + D + N – Nmean**
- **Photons received per voxel (x, Δx; y , Δy; t, Δt)**
- **3D plot, movie**
- **3D FPA plots, successive times**
- **2D FPA plots, successive times**
- **2D FPA matrices (numerical values), successive times**
- **Photons vs. angle and time**
- **Photons vs. angle, all times; vs. time, all angles**

Figure 4 shows model results giving the photon distribution versus delay time (after the arrival of the ballistic photons) and scattering factor g, for a point target; Figure 5 illustrates the photon distribution versus incident angle and g; and Figure 6 shows the photon distribution versus delay time, incident angle, and g. In Figures 4 and 5, the color scale indicates the fraction of photons in the bin. Each row represents a histogram with total value 1.0; since there are 100 rows, the total of the color-scale value over the figure is 100. It may be seen that, for the parameters assumed (R = 100 m, R/L = 4), for $g \leq 0.9$, the typical delay is greater than 1 nsec and the typical incident angle (angle between photon direction and normal to aperture) is greater than 5 deg. In Figure 6, the incident angle is translated into "pixels away," that is, the distance between the center of the FPA and the detector recording the photon, measured in pixel diameters. It may be seen that for $g < 0.9$, most photons arrive more than 100 pixels from the FPA center and with a delay time greater than 1 nsec. For $g = 0.99$, the opposite is true.

If the beam divergence were small, then many outward-bound photons, even though they had been scattered, could still strike the target, thus increasing the estimated value of N_b given by (1). Model results illustrating this effect are given in Figure 7, under the assumptions used to compute the results (R = 100 m, R/L = 4, g = 0.99; see Section 6). Our target's 70 cm diameter subtends an angle, as seen from the lidar, of ±3.5 mrad (0.35 m)/(100 m). Figure 7 shows that the fraction of outgoing beam that scatters but still strikes the target is ~ 5% of the outward-bound scattered photons. About 2% (= $e^{-R/L}$) of the outward-bound photons are ballistic. A correction to the results in Section 6 could be made for this effect; we have not done so here.

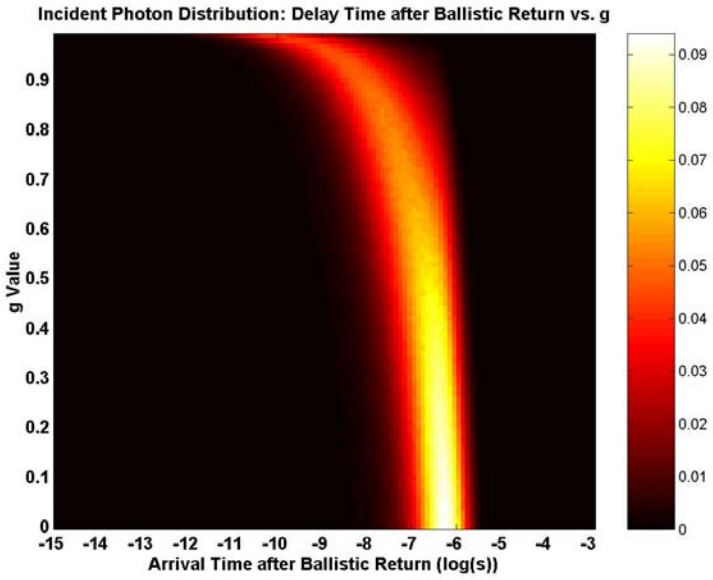

R = 100 m, R/L = 4. For g $\leq$ 0.9, Typical Delay $\geq$ 1 nsec.

Figure 4. Photon Distribution versus Delay Time and Scattering Factor

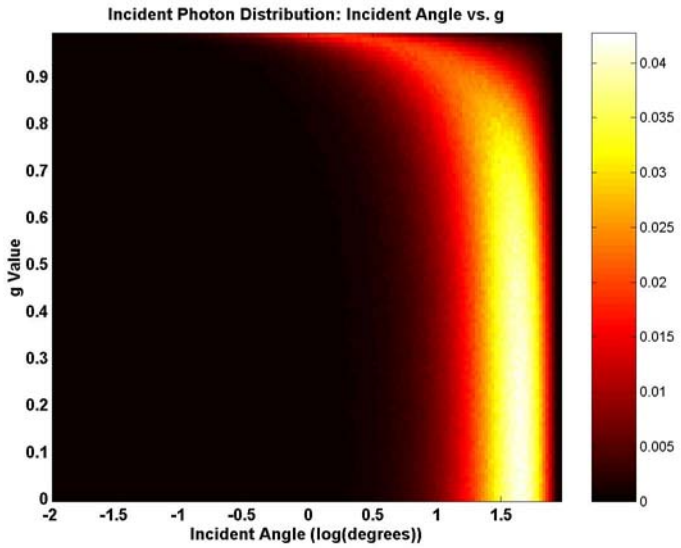

R/L = 4. For g $\leq$ 0.9, Typical Incident Angle $\geq$ 5 deg.

Figure 5. Photon Distribution versus Incident Angle and Scattering Factor

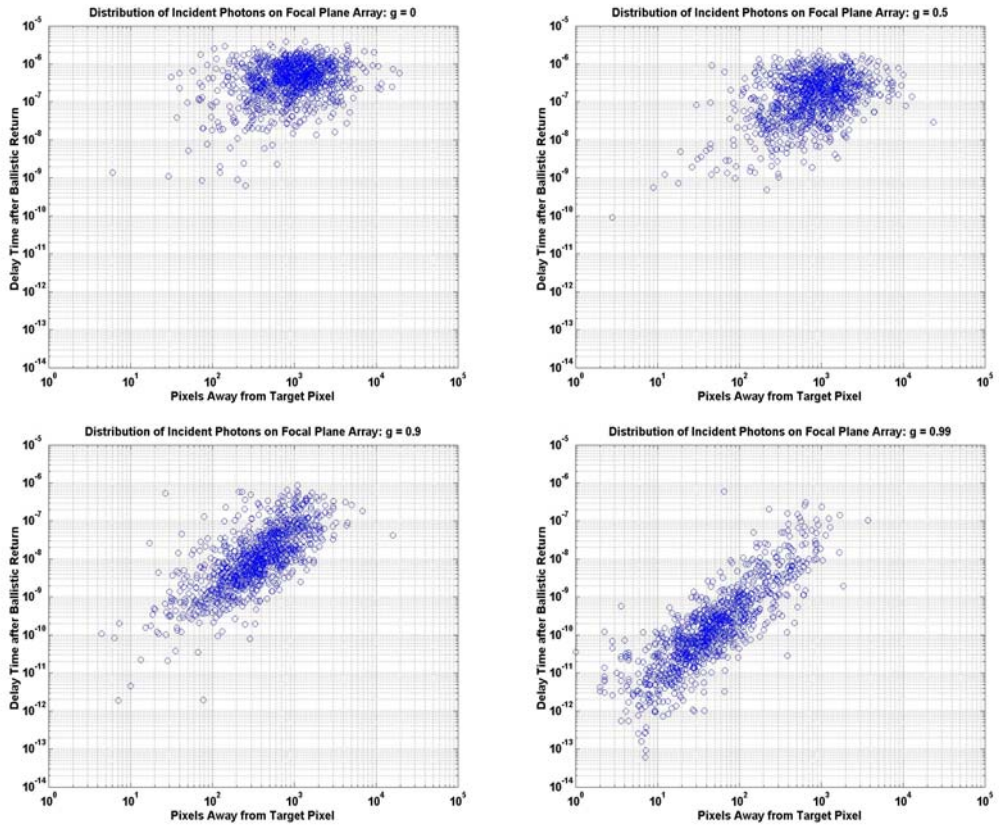

Figure 6. Photon Distribution versus Delay Time, Pixel Location, and Scattering Factor

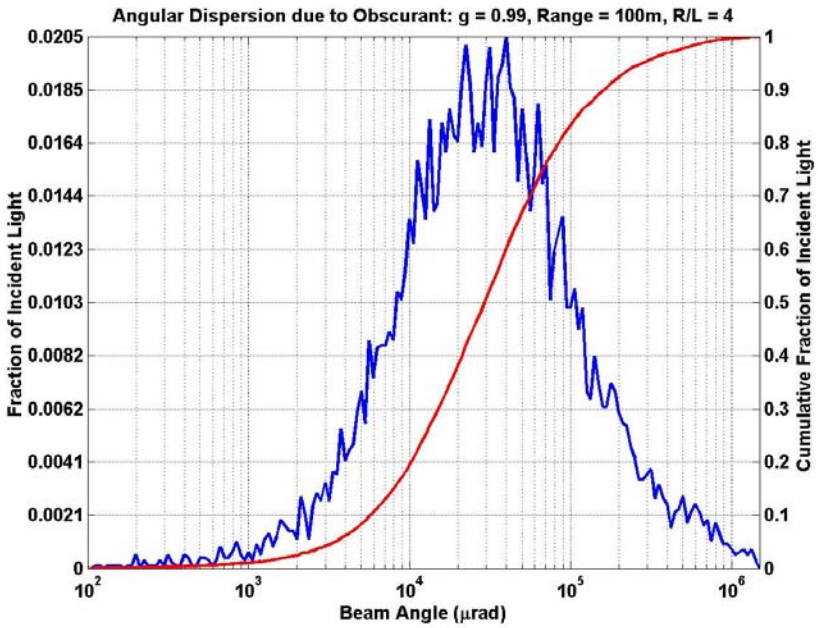

Figure 7. Photon Distribution versus Beam Angle (left scale corresponds to jagged line; right scale corresponds to smooth line)

5. OTHER CONSIDERATIONS

5.1 FORWARD SCATTERING

The HG function underestimates the number of scattered photons very near the forward direction. More exact phase functions should be used for detailed estimates. For this reason we assume $g = 0.99$ for the highly forward scattering considered herein, rather than $g \sim 0.9$, as indicated in Figure 3.

The effect is related to the forward-scattering phenomenon encountered in classical electromagnetic (EM) scattering theory. For near-isotropic scattering from a sphere of radius a, Jackson [10], p. 451, states:

> The scattering in the forward direction is a typical diffraction pattern with a central maximum and smaller secondary maxima [Bessel function pattern], while at larger angles it is isotropic… The total scattering cross section is obtained by integrating over all angles. Neglecting the interference terms, we find…that the shadow diffraction peak [width ~ $\lambda/2\pi a$] gives a contribution of πa^2, and so does the isotropic part. The total scattering cross section is thus $2\pi a^2$.

5.2 THERMAL PHOTONS

We estimate the number of thermal photons that are received at a detector (individual pixel) during a time gate. Because the optics are presumably at approximately room temperature, we make the approximation that the detector (area = w^2, neglecting the fill factor) is at the center of a hemisphere of radius R with an inner surface at temperature 300 K and emissivity of unity. The thermal emission from the hemisphere is given by the well-known Planck function

$$B(f) = \varepsilon \frac{2hf^3}{c^2} \frac{1}{\left(e^{hf/kT} - 1\right)} \text{ W m}^{-2} \text{ Hz}^{-1} \text{ sr}^{-1} \quad , \tag{5}$$

where h, k, and c are Planck's constant, Boltzmann's constant, and the speed of light respectively, $f = c/\lambda = 194$ THz, $T = 300$ K, and ε = emissivity = 1. The number of thermal photons per pixel expected in a time bin is then independent of R:

$$Nppix_{th} = \frac{B(f)\Delta f \cdot \delta t \cdot \eta}{\left(\frac{hc}{\lambda}\right)} \cdot \frac{w^2}{R^2} \cdot \int_0^{2\pi} d\phi \int_0^{\pi/2} R^2 \sin\theta d\theta \cdot \cos\theta$$
$$= \frac{\pi B(f) \cdot \Delta f \cdot \delta t \cdot \eta w^2}{\left(\frac{hc}{\lambda}\right)} \quad , \tag{6}$$

where Δf = bandwidth, assumed to be 630 GHz (corresponding to $\Delta\lambda = 5$ nm), δt = time bin = 1 ns. For the assumed lidar, $Nppix_{th} = 1.3 \times 10^{-8}$ photons, entirely negligible.

5.3 SOLAR PHOTONS

The intensity of sunlight at Earth at 1.54 μm is $F_{solar} \sim 270$ W m^{-2} μm^{-1} ([11], p. 172). We conservatively neglect atmospheric absorption (it is negligible in clear air -- [11], p. 122) or any obscurant. We consider direct sunlight falling on the target and undergoing Lambertian scattering into 2π steradians. We assume that the scattering plane is the *xy* plane, and that the sun and the lidar are both near the *z* axis at small values of θ. In this case the fraction of emitted energy that strikes the aperture is $\sim\Omega_{rcv}/\pi$, where Ω_{rcv} is the solid angle subtended by the lidar aperture, as seen from the target. The estimated number of solar photons striking an individual detector during a time gate is

$$N_{solar} = \frac{F_{solar}}{\left(\frac{hc}{\lambda}\right)} (R \cdot IFOV)^2 \cdot \Delta\lambda \cdot \delta t \cdot \frac{\Omega_{rcv}}{\pi} \rho \cdot \eta \quad . \tag{7}$$

As with (6) for thermal photons, the expression for N_{solar} is also independent of R.

For the parameters assumed in Section 6, N_{solar} equals 0.05 photons. For the linear detector we may neglect this, especially since direct sunlight is unlikely when obscurants are present. For the Geiger detector, a continuous illumination by solar photons can reduce the effective number of photons recorded, especially for scatterers located relatively deep in the target compared with the front scatterers.

6. RESULTS

Monte Carlo results were computed for a simulated target consisting of 11 points in 3D space arranged approximately in the shape of a small "car," as shown in Figure 8. The points may be thought of, schematically, as two front wheels, two headlights, one hood ornament, two top corners of the windshield, two top corners at the rear, and two rear wheels. The coordinate system used is

z = longitudinal axis of target ("car") = axis of lidar = line between lidar and target)

x = horizontal axis, that is, the left front and the left rear "wheels" have the same x value

y = vertical axis, that is, both "headlights" have the same y value

To prevent one point from shadowing another, the 11 locations are chosen such that no two points have exactly the same values of n_x ,n_y. The time bin Δt is taken to be 0.5 nsec; the pixel depth = $\Delta z = c\Delta t/2$ = 7.5 cm = $\Delta x = \Delta y$.

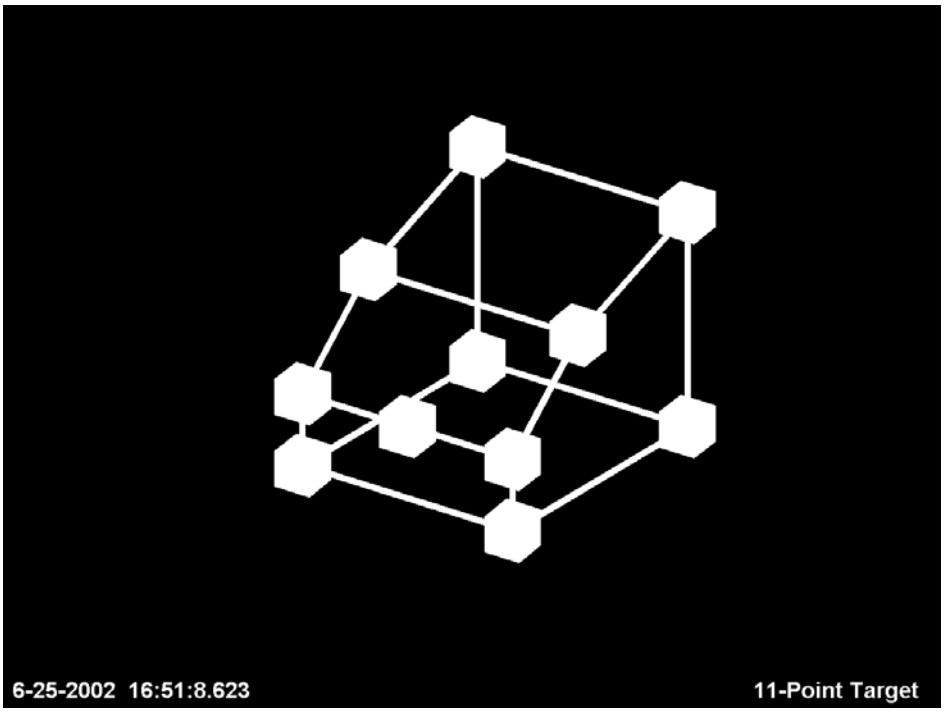

Figure 8. The Target Model: "Car" Consisting of 11 Points

Figures 9–12 are presented as a computer-printed summary of parameters used for the model run, and resulting "quad-charts" showing:

- top-left: ballistic photons
- top-right: ballistic + diffuse photons (B + D)
- bottom-left: ballistic + diffuse + noise photons (B + D + N)
- bottom-right: ballistic + diffuse + noise photons, minus noise mean (B + D + N – Nmean)

The detailed assumptions are provided in the computer output at the top of Figures 9–12. In summary, we assumed

- R = 100 m
- an optical depth = R/L = 4 (slightly greater than the "visibility" condition of (3.912)L).
- Nmean = 100 for the linear detector (see [12]) and $5*10^{-7}$ for the Geiger detector [13, p. 340]
- E = 0.04 J for the linear detector, 0.0004 J for the Geiger detector
- a PRF of 100 Hz for the linear-detector lidar and 10,000 Hz for the Geiger-detector lidar; both have average radiated power = 4 watts
- integration times of 10 and 100 msec.
- Geiger recovery time > 10 nsec and < 100 μsec ([14], p. 353)

Results are summarized as follows. Color scale represents number of photons recorded, and varies with each plot.

- Figure 9: Linear Detector, 10 msec integration time (1 pulse):
- Figure 10: Linear Detector, 100 msec integration (10 pulses)
- Figure 11: Geiger Detector, 10 msec integration time (100 pulses): Note that deep scatterers are often not as bright as front scatterers, since sometimes a diffuse photon from a front scatterer will trigger the Geiger detector, thereby precluding detection of a subsequent photon from a deeper scatterer on the same pulse.
- Figure 12: Geiger Detector, 100 msec integration time (1,000 pulses)

For the parameters assumed, the results indicate the following. For the linear detector, integration over 10 msec (1 pulse) is insuffucient to produce a meaningful 3D image, whereas integration over 100 msec (10 pulses) does produce a meaningful image. For the Geiger detector, integration over 10 msec (100 pulses) is suffucient to produce a

meaningful image, and integration over 100 msec (1,000 pulses) produces a very clear image.

If image quality metrics (IQMs) are developed for flash lidar images of targets in obscurants, we suggest that since the effects of multiple target points are important (diffuse photons from one target point affect the appearance of other target points), a standard 3D multipoint target be used. This is analogous to the standard U.S. Air Force bar chart for evaluating electro-optical/infrared imagery. Key inputs to IQMs for various lidars could include (1) the full-widths at half maximum (FWHM) in x, y, and z of the single-point 3D point-spread function (PSF), caused by diffuse scattering; (2) the signal-to-interference-plus-noise ratio (SINR); and (3) the gray-scale fidelity.

Flash Lidar, Monte Carlo Simulation Parameters: Linear Detectors

Environmental Parameters:

Range (R) = 100 m
Scattering Length (L) = 25 m
R/L = 4
Target Reflectivity (ρ) = 0.1
2-way Delay Time = 0.66713 μs
Anisotropy Factor (g) = 0.99
Scattering Albedo (α) = 1

Lidar Parameters:

Pulse Energy = 0.04 J
Wavelength = 1.54 μm
Photons/Pulse = 3.100966e+017
Overall Efficiency (η) = 0.1
Number of Pulses Integrated: 1
Dwell Time: 10 ms
Pulse Repetition Frequency (PRF): 100 Hz

Detector Parameters:

Aperture Diameter (D) = 6 cm
Focal Length = 6.67 cm
f number = 1.1117
Pitch = 50 μm
IFOV = 749.6252 μrad
Target x-dim = 9 pixels
Target y-dim = 9 pixels
Outgoing Beam x-dim = 32 pixels
Outgoing Beam y-dim = 32 pixels

Voxel Resolution:

Width Resolution = 7.4963 cm
Height Resolution = 7.4963 cm
Depth Resolution = 7.4948 cm = 0.5 ns
diffraction limit = 0.31313 cm

Results for Single-Point-Target:

Photons: Incident on Aperture = 1248
Photons: Expected Ballistic = 22.8572
Photons Collected: Ballistic = 26
Photons Collected: Ballistic + Diffuse = 91
Photons Collected: Ballistic + Diffuse + Noise = 730

Results for 11 Point "Car" Target:

Photons: Incident on Aperture = 13728
Photons: Expected Ballistic = 251.4296
Photons Collected: Ballistic = 274
Photons Collected: Ballistic + Diffuse = 965
Photons Collected: Ballistic + Diffuse + Noise = 738

6-19-2003 16:51:8.742

Runtime: 0 day(s); 0 hour(s); 0 minute(s); 46.109 secon

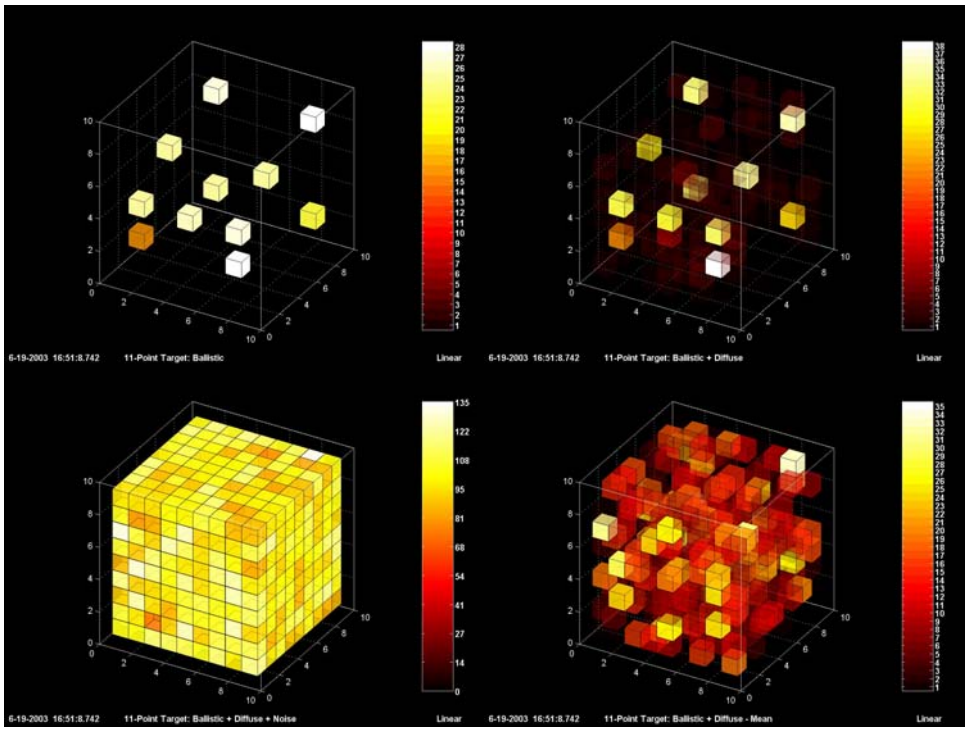

Figure 9. Parameters and Results for Linear Detector, 10 msec Integration Time (1 Pulse)

Flash Lidar, Monte Carlo Simulation Parameters: Linear Detectors

Environmental Parameters:

Range (R) = 100 m
Scattering Length (L) = 25 m
R/L = 4
Target Reflectivity (ρ) = 0.1
2-way Delay Time = 0.66713 μs
Anisotropy Factor (g) = 0.99
Scattering Albedo (α) = 1

Lidar Parameters:

Pulse Energy = 0.04 J
Wavelength = 1.54 μm
Photons/Pulse = 3.100966e+017
Overall Efficiency (η) = 0.1
Number of Pulses Integrated: 10
Dwell Time: 100 ms
Pulse Repetition Frequency (PRF): 100 Hz

Detector Parameters:

Aperture Diameter (D) = 6 cm
Focal Length = 6.67 cm
f number = 1.1117
Pitch = 50 μm
IFOV = 749.6252 μrad
Target x-dim = 9 pixels
Target y-dim = 9 pixels
Outgoing Beam x-dim = 32 pixels
Outgoing Beam y-dim = 32 pixels

Voxel Resolution:

Width Resolution = 7.4963 cm
Height Resolution = 7.4963 cm
Depth Resolution = 7.4948 cm = 0.5 ns
diffraction limit = 0.31313 cm

Results for Single-Point-Target:

Photons: Incident on Aperture = 12480
Photons: Expected Ballistic = 228.5724
Photons Collected: Ballistic = 223
Photons Collected: Ballistic + Diffuse = 903
Photons Collected: Ballistic + Diffuse + Noise = 729

Results for 11 Point "Car" Target:

Photons: Incident on Aperture = 137280
Photons: Expected Ballistic = 2514.2962
Photons Collected: Ballistic = 2497
Photons Collected: Ballistic + Diffuse = 9201
Photons Collected: Ballistic + Diffuse + Noise = 738

6-20-2003 10:22:38.109

Runtime: 0 day(s); 0 hour(s); 3 minute(s); 4.859 second

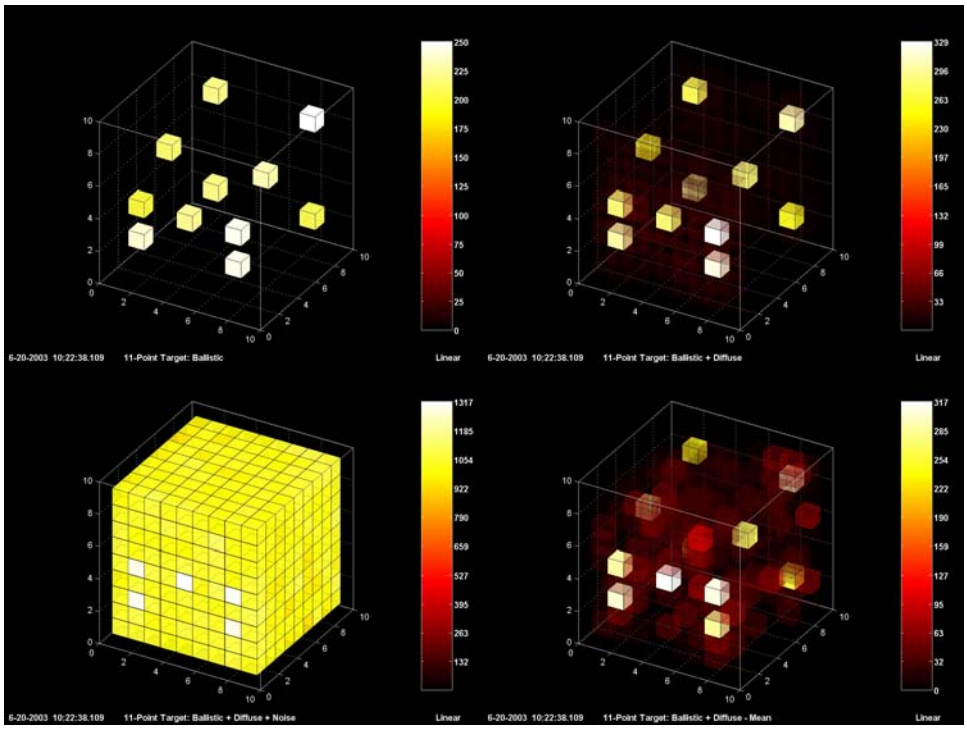

Figure 10. Parameters and Results for Linear Detector, 100 msec Integration Time (10 Pulses)

Flash Lidar, Monte Carlo Simulation Parameters: Geiger Detectors

Environmental Parameters:

Range (R) = 100 m
Scattering Length (L) = 25 m
R/L = 4
Target Reflectivity (ρ) = 0.1
2-way Delay Time = 0.66713 μs
Anisotropy Factor (g) = 0.99
Scattering Albedo (α) = 1

Lidar Parameters:

Pulse Energy = 0.0004 J
Wavelength = 1.064 μm
Photons/Pulse = 2.14248578541128e+015
Overall Efficiency (η) = 0.1
Number of Pulses Integrated: 100
Dwell Time: 10 ms
Pulse Repetition Frequency (PRF): 10000 Hz

Detector Parameters:

Aperture Diameter (D) = 6 cm
Focal Length = 13.34 cm
f number = 2.2233
Pitch = 100 μm
IFOV = 749.6252 μrad
Target x-dim = 9 pixels
Target y-dim = 9 pixels
Outgoing Beam x-dim = 32 pixels
Outgoing Beam y-dim = 32 pixels

Voxel Resolution:

Width Resolution = 7.4963 cm
Height Resolution = 7.4963 cm
Depth Resolution = 7.4948 cm = 0.5 ns
diffraction limit = 0.21635 cm

Results for Single-Point-Target:

Photons: Incident on Aperture = 900
Photons: Expected Ballistic = 15.7923
Photons Collected: Ballistic = 23
Photons Collected: Ballistic + Diffuse = 85
Photons Collected: Ballistic + Diffuse + Noise = 85

Results for 11 Point "Car" Target:

Photons: Incident on Aperture = 9900
Photons: Expected Ballistic = 173.715
Photons Collected: Ballistic = 186
Photons Collected: Ballistic + Diffuse = 613
Photons Collected: Ballistic + Diffuse + Noise = 613

6-20-2003 11:5:38.109

Runtime: 0 day(s); 0 hour(s); 0 minute(s); 29.969 secon

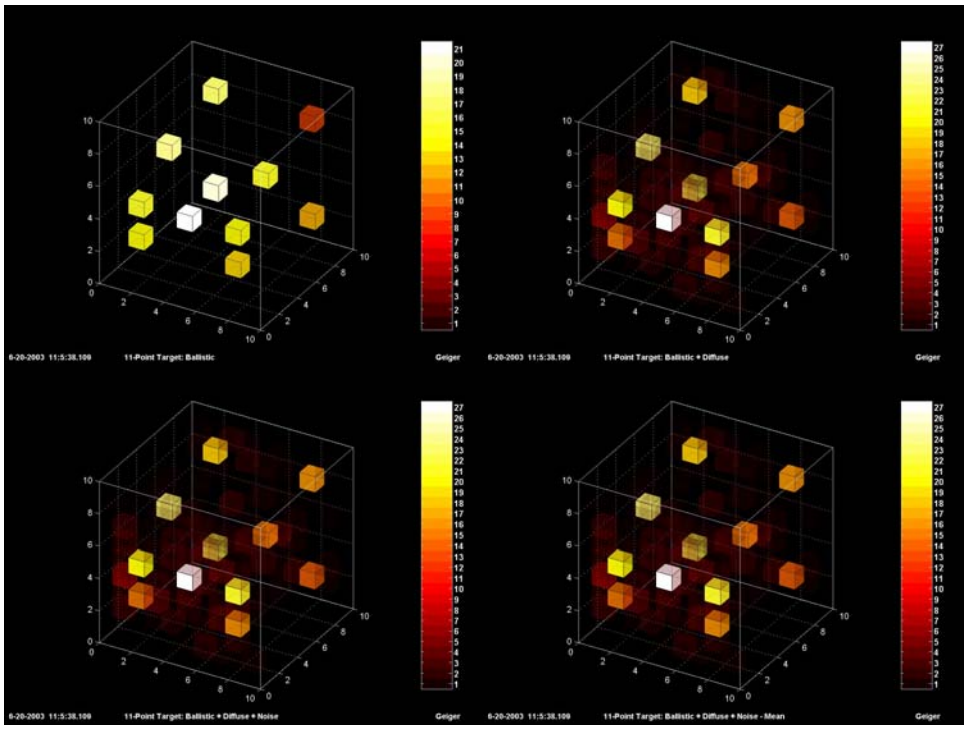

Figure 11. Parameters and Results for Geiger Detector, 10 msec Integration Time (100 Pulses)

Flash Lidar, Monte Carlo Simulation Parameters: Geiger Detectors

Environmental Parameters:

Range (R) = 100 m
Scattering Length (L) = 25 m
R/L = 4
Target Reflectivity (ρ) = 0.1
2-way Delay Time = 0.66713 μs
Anisotropy Factor (g) = 0.99
Scattering Albedo (α) = 1

Lidar Parameters:

Pulse Energy = 0.0004 J
Wavelength = 1.064 μm
Photons/Pulse = 2.14248578541128e+015
Overall Efficiency (η) = 0.1
Number of Pulses Integrated: 1000
Dwell Time: 100 ms
Pulse Repetition Frequency (PRF): 10000 Hz

Detector Parameters:

Aperture Diameter (D) = 6 cm
Focal Length = 13.34 cm
f number = 2.2233
Pitch = 100 μm
IFOV = 749.6252 μrad
Target x-dim = 9 pixels
Target y-dim = 9 pixels
Outgoing Beam x-dim = 32 pixels
Outgoing Beam y-dim = 32 pixels

Voxel Resolution:

Width Resolution = 7.4963 cm
Height Resolution = 7.4963 cm
Depth Resolution = 7.4948 cm = 0.5 ns
diffraction limit = 0.21635 cm

Results for Single-Point-Target:

Photons: Incident on Aperture = 9000
Photons: Expected Ballistic = 157.9227
Photons Collected: Ballistic = 164
Photons Collected: Ballistic + Diffuse = 670
Photons Collected: Ballistic + Diffuse + Noise = 67(

Results for 11 Point "Car" Target:

Photons: Incident on Aperture = 99000
Photons: Expected Ballistic = 1737.1501
Photons Collected: Ballistic = 1836
Photons Collected: Ballistic + Diffuse = 6207
Photons Collected: Ballistic + Diffuse + Noise = 62(

6-20-2003 11:15:36.734

Runtime: 0 day(s); 0 hour(s); 4 minute(s); 20.016 secon

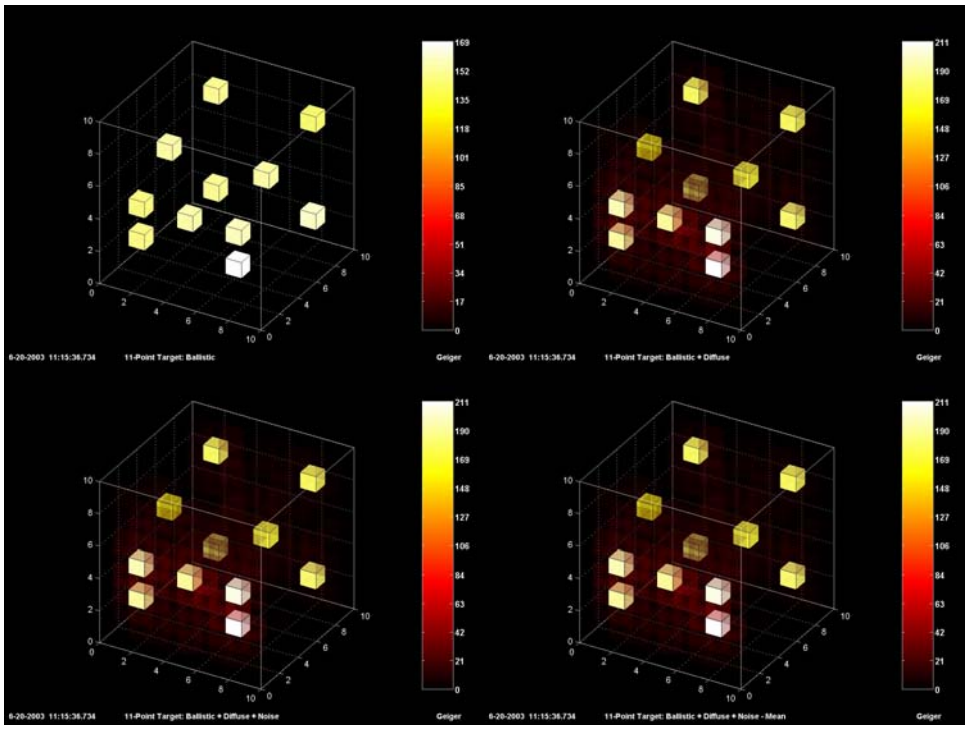

Figure 12. Parameters and Results for Geiger Detector, 100 msec Integration Time (1,000 Pulses)

7. POST-PROCESSING OF GEIGER RESULTS

The one count maximum per pulse per pixel in a Geiger avalanche photodiode (APD) imaging array results in two observed phenomena when multiple pulses are integrated: (1) the intensity distribution of the incident light does not linearly map to the output of the detector, (2) in the 3D image, the intensity of "later" voxels (greater delay time) can be suppressed by returns in "earlier" voxels with the same pixel coordinates.

We may compare the expected number of received counts from linear and Geiger detectors as follows. The number of ballistic photons received per pulse is Poisson distributed with mean $\mu_{\text{ballistic}}$:

$$P\left(N_{ballistic}\right) = \frac{\mu_{ballistic}^{N_{ballistic}}}{N_{ballistic}!} e^{-\mu_{ballistic}} \quad . \tag{8}$$

For the linear detector

$$\mu_{counts} = N_{pulses}\mu_{ballistic}, \quad \sigma^2 = \mu_{counts} \quad . \tag{9}$$

The output initiated by one photon incident on a Geiger detector element is assumed to be indistinguishable from that produced by several incident photons. Therefore, the output from a Geiger detector element for one pulse is reduced to a Bernoulli trial where "success" (a count in this case) can be defined as 1 or more ballistic photons received and we denote the probability of that event by *p*. The distribution is binomial with mean *np* and variance $np(1-p)$, where $n = N_{pulses}$:

$$\begin{aligned} p &= P(N_{ballistic} \geq 1) = 1 - e^{-\mu_{ballistic}} \\ \mu_{counts} &= N_{pulses}(1 - e^{-\mu_{ballistic}}) \\ \sigma^2 &= \mu_{counts}\, e^{-\mu_{ballistic}} \end{aligned} \quad . \tag{10}$$

Figure 13 illustrates expected counts for ideal linear and Geiger detectors. The output from the Geiger detector increasingly diverges from that of the linear detector as $\mu_{ballistic}$ increases.

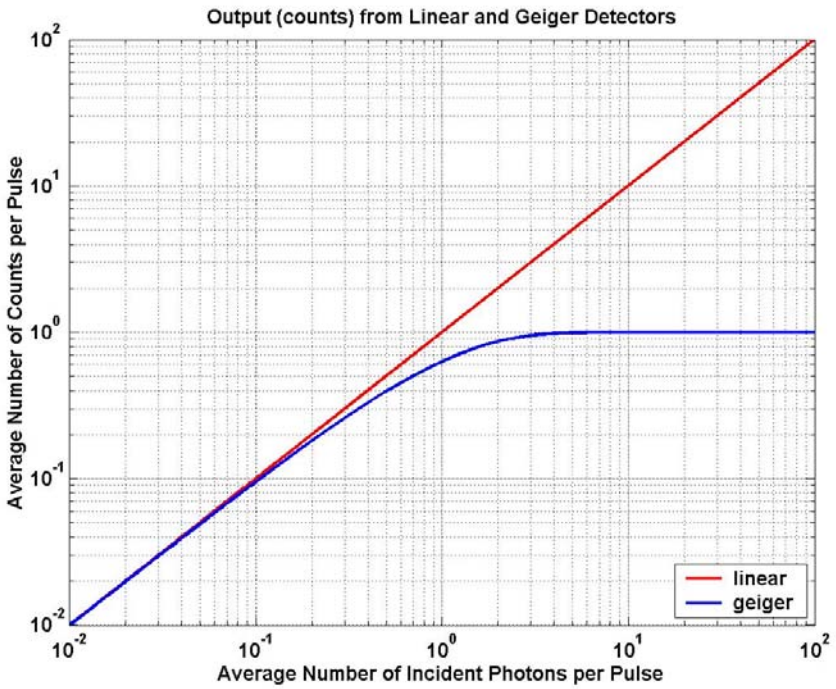

Figure 13. Output (Counts) from Linear and Geiger Detectors

In order to study the effect of the difference in output between the two detector classes, consider an image with two pixels: *Br* and *Dm*. Pixel *Br* is brighter than pixel *Dm* when the image is obtained in linear mode, by a ratio known as the *contrast ratio CR(Br,Dm)*. For the linear detector,

$$CR_L(Br,Dm) = \frac{\mu_{counts}(Br)}{\mu_{counts}(Dm)} = \frac{\mu_{photons}(Br)}{\mu_{photons}(Dm)} \quad . \tag{11}$$

For a Geiger detector, the measured contrast ratio between the same two regions is:

$$CR_G(Br,Dm) = \frac{\mu_{counts}(Br)}{\mu_{counts}(Dm)} = \frac{\left(1-e^{\mu_{photons}(Br)}\right)}{\left(1-e^{\mu_{photons}(Br)/CR_L(Br,Dm)}\right)} \quad . \tag{12}$$

Figure 14 shows the relationship between various values of CR_G and $\mu_{photons}(Br)$.

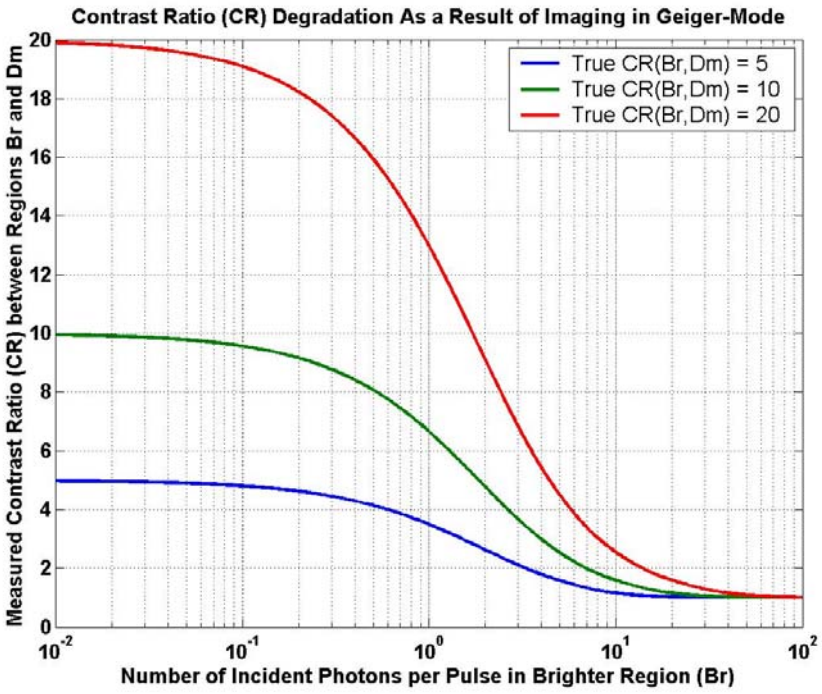

Figure 14. Geiger Detector: Contrast Ratio of Image

To help remedy the degradation in *CR* resulting from the detector saturation described by (12), a Geiger image may be remapped to a scale more proportional to the number of incident photons. Solving (10) for $\mu_{ballistic}$ and multiplying by N_{pulses}, we have

$$N_{remapped} = N_{pulses}\mu_{ballistic} = -N_{pulses}\ln\left(1-\frac{\mu_{counts}}{N_{pulses}}\right) \quad . \tag{13}$$

We presumably have only one image and therefore do not know μ_{counts} for each pixel; we thus replace μ_{counts} with our best guess, N_{counts}. Figure 15 illustrates this Geiger remapping technique.

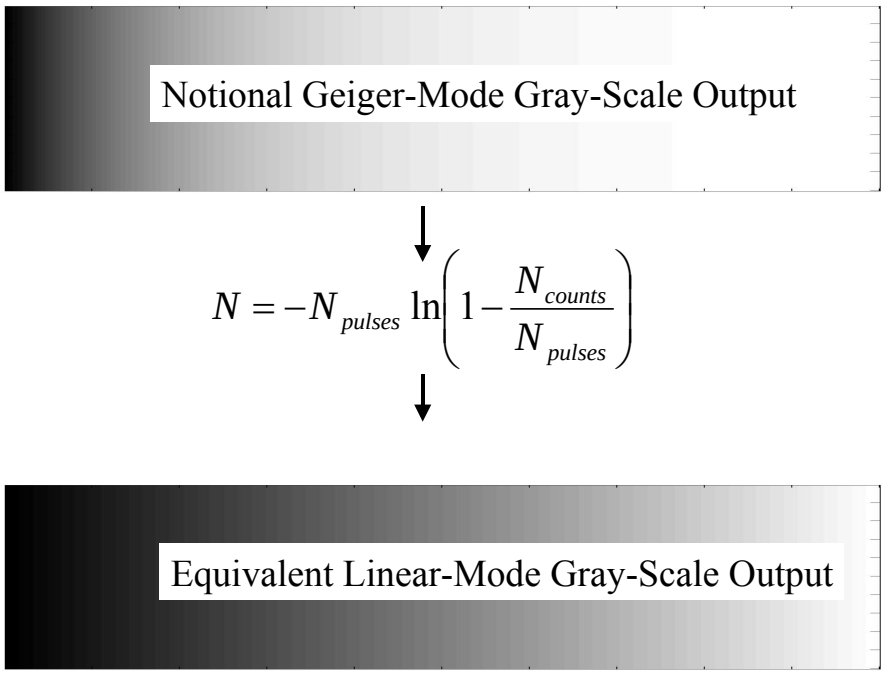

Figure 15. Geiger Remapping Technique

Applying (13) to a 3D image requires accounting for the recovery time needed by the detector elements after being triggered. For simplicity, we assume the recovery time T_R corresponds to a greater depth than the maximum depth to which the target is being imaged. This latter depth corresponds to some number of time-bins n_t. In this case, as soon as an element is triggered for a voxel located at x_i,y_j,t_k, the voxels "behind" that one ($x_i,y_j,t_{k+1}\ldots x_i,y_j,t_{nt}$) will be unresponsive to any incident photons arriving from the target resulting from the current laser pulse. Therefore, when remapping the counts accumulated in a given voxel, a better value of N_{pulses} to use in (13), which will be called the *effective number of pulses integrated* or N_{pulses}*, is simply:

$$N^*_{pulses}\left(x_i, y_j, t_k\right) = N_{pulses} - \sum_{l=1}^{k-1} N_{counts}\left(x_i, y_j, t_l\right) \quad . \tag{14}$$

N_{counts} (x_i, y_j, t_l) is either 0 or 1. The correction is not exact, since a "1" may sometimes indicate more than one count. However, the remapping technique is quite useful. Figure 16 depicts three-dimensional images before and after remapping and shows that the results of Geiger remapping can result in an image that is much easier for a human to interpret than the corresponding raw (non-remapped) image.

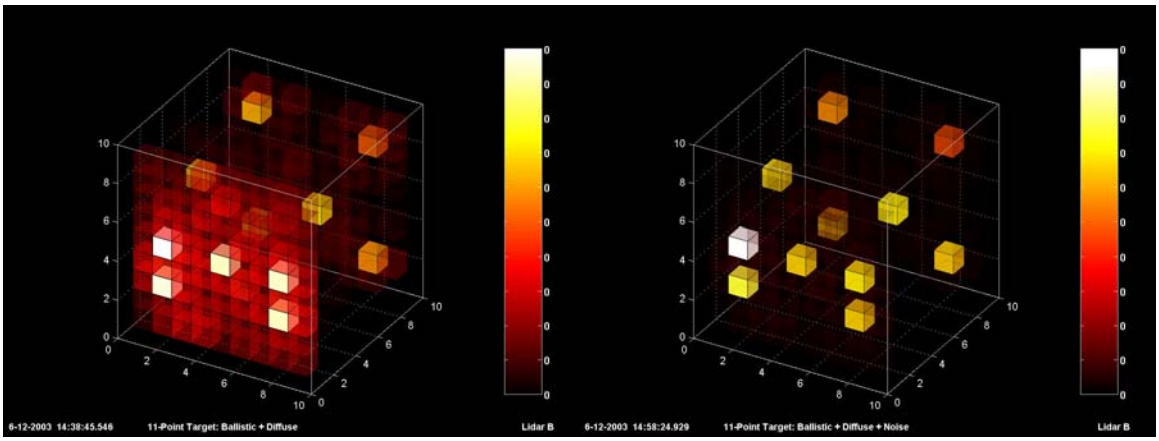

Figure 16. Three-Dimensional Geiger Images: Raw and Remapped

Finally, if a detector element at coordinate x_i,y_j in the imaging array is continuously illuminated (e.g., by solar radiation) at a level of $\mu_{photons}$ per time bin, whether or not that element is available to be triggered in voxel x_i,y_j,t_k depends on whether or not it was triggered in any of the preceding voxels: $x_i,y_j,t_1,\ldots,x_i,y_j,t_{k-1}$. This is equivalent, once again, to a Bernoulli trial where "success" can be defined as "untriggered." The probability that a detector element is untriggered at t_k is:

$$p_{untriggered}\left(x_i, y_j, t_k\right) = P\left(N_{photons}\left(x_i, y_j, t_1\right) = 0, \ldots, N_{photons}\left(x_i, y_j, t_{k-1}\right) = 0\right) \quad , \qquad (15)$$

and $P(N_{photons}(x_i,y_j,t_l) = 0)$ is the "q" (1-p) to the p given in (12). Therefore,

$$p_{untriggered}\left(x_i, y_j, t_k\right) = q^{k-1} = e^{-\mu_{photons}(k-1)} \quad . \qquad (16)$$

The average effective number of pulses integrated for voxel x_i,y_j,t_k is

$$N^*_{pulses}\left(x_i, y_j, t_k\right) = N_{pulses} e^{-\mu_{photons}(k-1)} \quad . \qquad (17)$$

N_{pulses}* under various levels of continuous illumination is shown in Figure 17. The average number of counts expected from a portion of the target located in voxel x_i,y_j,t_k then decreases along with N_{pulses}*.

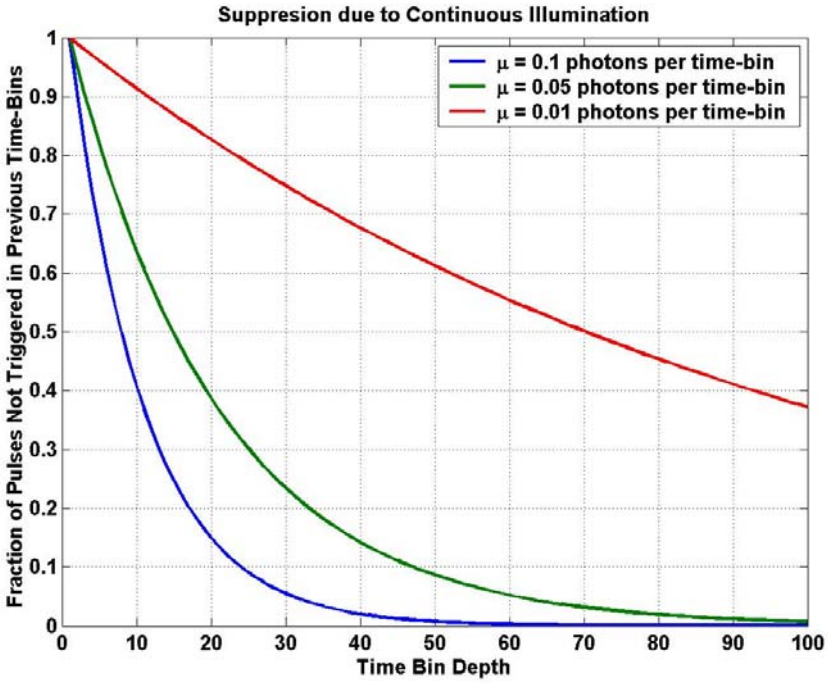

Figure 17. Geiger Detector: Eclipsing Effect in Late Time Bins

8. COMPARISON WITH DIFFUSION THEORY

In this section we discuss a comparison of the Monte Carlo results with results from diffusion theory. The following summary is for all scattering angles, for $R/L >> 1$, which we compare to our Monte Carlo results.

8.1 DIFFUSION EQUATION—PARTICLE FLOW

The simple diffusion equation for particle flow is obtained as follows ([15], p. 4). The particle flow (or probability current density) q (m^{-2} s^{-1}) is given by

$$q = -D\nabla\rho \quad , \tag{18}$$

where D is the diffusion coefficient (m^2 s^{-1}) and ρ is the particle density (m^{-3}). From the equation of continuity

$$\nabla \cdot q = -\frac{\partial \rho}{\partial t} \quad , \tag{19}$$

we have

$$\nabla^2 \rho = \frac{1}{D}\frac{\partial \rho}{\partial t} \quad , \tag{20}$$

which is the diffusion equation.

8.2 GREEN FUNCTION SOLUTION

For this theoretical discussion we take $t = 0$ as the time the pulse leaves the (point) target. For an infinite uniform medium and an impulse at $\mathbf{r} = 0$, $t = 0$, corresponding to the laser pulse just leaving the target, the mathematical conditions are

$$\rho_0(\mathbf{r}, 0) = \delta(\mathbf{r}), \quad \rho_0(\infty, t) = 0 \quad , \tag{21}$$

and the solution ([15], p. 29; [16], p. 868) is

$$\rho_0(r, t) = \frac{1}{(4\pi D t)^{3/2}} e^{-r^2/4Dt} \quad . \tag{22}$$

The solution is simply a spherically symmetric Gaussian with a variance that grows linearly with time; (22) is also known in some communities as the Smirnov density ([17], Vol. 1, p. 206). Normalization is

$$\int_0^{4\pi} d\Omega \int_0^{\infty} dr \cdot \rho_0(r,t) = 1 \tag{23}$$

For isotropic scattering, $D = cL/3$, where L is the scattering length = mean free path, while for non-isotropic scattering, $D = cL/(3(1-\langle\cos\theta\rangle))$ [18]. This relation for the diffusion constant is derived in Appendix C. For the Henyey-Greenstein approximation, it is easily shown that $\langle\cos\theta\rangle = g$, where $\langle\ \rangle$ indicates an ensemble average over the distribution. For long times, the density decays as $t^{-3/2}$.

8.3 TOTAL PARTICLE EXIT RATE PAST *r = R*

The expected number of particles in a sphere of radius R at time t is given by

$$P(R,t) = \int_0^R dr \cdot 4\pi r^2 \cdot \rho_0(r,t) \quad . \tag{24}$$

Then the total rate (s^{-1}) at which particles exit the sphere $r = R$ is given by

$$F_0(t) = -\frac{\partial}{\partial t} \int_0^R dr \cdot 4\pi r^2 \cdot \rho_0(r,t) \quad . \tag{25}$$

Substituting (22) into (24) and carrying out the necessary operations yields an exit rate of

$$F_0(t) = \frac{R^3}{4\pi^{1/2} D^{3/2} t^{5/2}} e^{-R^2/4Dt} \quad , \tag{26}$$

which, for long times, decays as $t^{-5/2}$.

8.4 "FIRST–PASSAGE" EXIT RATE THROUGH *r = R*

In our Monte Carlo model, when a photon exits the sphere with radius $r = R$, it is removed from the system and cannot return to the inside of the sphere. Thus we model the "first-passage time" through $r = R$ [17] and the corresponding first-passage exit rate. The first-passage particle density inside the sphere is denoted $\rho_1(r,t)$. As discussed in [17], this is the solution to the diffusion equation (20) when an absorbing barrier is placed at $r=R$; the appropriate boundary condition at R can be shown to be $\rho_1(R,t)= 0$. We find $\rho_1(r,t)$ using classical separation-of variables. We have

$$\frac{\partial \rho}{\partial t} = D\nabla^2 \rho = \frac{D}{r} \frac{\partial^2}{\partial r^2} (r\rho) \quad . \tag{27}$$

We define

$$\rho_1(r,t) \equiv U(r)T(t), \quad U(R) = 0 \quad . \tag{28}$$

Then

$$\frac{1}{DT}\frac{dT}{dt} = \frac{1}{Ur}\frac{d^2}{dr^2}(rU) = const \equiv -k^2 \quad . \tag{29}$$

The solution for T is

$$T \sim e^{-Dk^2 t} \quad . \tag{30}$$

We set $u(r) = rU(r)$. Then

$$\begin{aligned} &\frac{d^2u}{dr^2} + k^2 u = 0 \\ &u(r) = \sum_n (A_n \sin(kr) + B_n \cos(kr)) \end{aligned} \quad . \tag{31}$$

Since $u \to 0$ as $r \to 0$, $B_n = 0$ for all n. Since $U(\mathrm{R}) = 0$, $u(\mathrm{R}) = 0$; thus $k_n R = n\pi$, and

$$\rho_1(r,t) = \sum_{n=1}^{\infty} \frac{A_n}{r} \sin\left(\frac{n\pi r}{R}\right) \exp\left(-Dt\left(\frac{n\pi}{R}\right)^2\right) \quad . \tag{32}$$

To compute the A_n, we note that

$$\int_0^R dr \cdot r \cdot \sin\left(\frac{m\pi r}{R}\right) \rho_1(r,0) = \frac{R}{\pi} \sum_{n=1}^{\infty} A_n \int_0^{\pi} du \sin(mu)\sin(nu) = \frac{R}{\pi} \sum_1^{\infty} A_n \delta_{nm} \cdot \frac{\pi}{2} = \frac{R}{2} A_m \quad . \tag{33}$$

$$A_m = \frac{2}{R} \int_0^R dr \cdot r \cdot \sin\left(\frac{m\pi r}{R}\right) \rho_1(r,0) = \frac{2}{4\pi R} \cdot \frac{m\pi}{R} \int_0^R 4\pi r^2 dr \frac{\sin\left(\frac{m\pi r}{R}\right)}{\left(\frac{m\pi r}{R}\right)} \delta(r) = \frac{m}{2R^2}$$

Then

$$\rho_1(r,t) = \frac{1}{2R^2} \sum_{n=1}^{\infty} \frac{n}{r} \sin\left(\frac{n\pi r}{R}\right) \exp\left(-Dt\left(\frac{n\pi}{R}\right)^2\right) \quad . \tag{34}$$

We now compute the first-passage time probability density F_1.

$$F_1(t) = -\frac{\partial}{\partial t} \int_0^R 4\pi r^2 dr \cdot \rho_1(r,t) = -4\pi \int_0^R r^2 dr \cdot \frac{\partial \rho_1}{\partial t} \quad . \tag{35}$$

$F_1(t)\, dt$ is the probability of exiting the sphere in the time interval $(t,\ t+dt)$; F_1 can therefore be interpreted as the rate (s^{-1}) at which particles exit the absorbing sphere ("exit rate") at $r = R$.

$$\frac{\partial \rho_1}{\partial t} = \frac{1}{2R^2}\sum_{n=1}^{\infty}\frac{n}{r}\sin\left(\frac{n\pi r}{R}\right)\left(\frac{-Dn^2\pi^2}{R^2}\right)\exp\left(-Dt\left(\frac{n\pi}{R}\right)^2\right)$$
$$= \frac{-D\pi^2}{2R^4}\sum_{n=1}^{\infty}\frac{n^3}{r}\sin\left(\frac{n\pi r}{R}\right)\exp\left(-Dt\left(\frac{n\pi}{R}\right)^2\right) \quad . \tag{36}$$

$$F_1(t) = \frac{2\pi^3 D}{R^4}\sum_{n=1}^{\infty} n^3 \exp\left(-Dt\left(\frac{n\pi}{R}\right)^2\right)\int_0^R dr \cdot r \cdot \sin\left(\frac{n\pi r}{R}\right) \quad . \tag{37}$$

The integral equals $(R^2/n\pi)(-1)^{n+1}$; thus

$$F_1(t) = \frac{2\pi^2 D}{R^2}\sum_{n=1}^{\infty}(-1)^{n+1} n^2 \exp\left(-Dt\left(\frac{n\pi}{R}\right)^2\right) \quad . \tag{38}$$

For long times, the $n = 1$ term dominates, and $F_1(t)$ decays exponentially as $\exp(-D\pi^2 t/R^2)$. This should be contrasted with the comparatively slow ($t^{-5/2}$) power-law exit rate (26), corresponding to the case where photons are *never* removed from the system.

The intensity (m^{-2} s^{-1}) of photons at R is

$$I(t) = \frac{N}{4\pi R^2} F_1(t) \tag{39}$$

We also note that for small angle scattering the diffusion constant becomes

$$D = \frac{cL}{3(1 - <\cos\theta>)} \cong \frac{cL}{3\left(1 - <1 - \frac{\theta^2}{2}>\right)} = \frac{cL}{3\left[1 - \left(1 - \frac{<\theta^2>}{2}\right)\right]} = \frac{2cL}{3<\theta^2>} \quad , \tag{40}$$

and the intensity becomes

$$I(t) = \frac{N\pi cL}{3R^4 <\theta^2>}\sum_{n=1}^{\infty}(-1)^{n+1} n^2 \exp\left[-\left(\frac{n\pi}{R}\right)^2 \frac{2cLt}{3<\theta^2>}\right] \quad . \tag{41}$$

This is somewhat different from the corresponding equation derived for an astrophysical situation by Alcock and Hatchett [19]; the differences are discussed in Appendix B.

8.5 TELEGRAPH EQUATION

The speed of light does not appear in the diffusion equation (20), and the solution implies that a small number of photons travel faster than c, which is clearly non-physical.

This situation may be remedied by use of the *telegraph equation* [20], which combines the diffusion and wave equations:

$$\nabla^2 \rho = \frac{1}{D}\frac{\partial \rho}{\partial t} + \frac{1}{c}\frac{\partial^2 \rho}{\partial t^2} \quad . \tag{42}$$

Morse and Feshbach ([16], p.868) give the Green function solution as

$$\rho_{0T}(r,0) = \delta(r), \qquad \rho_{0T}(\infty,t) = 0$$

$$\rho_{0T}(r,t) = \frac{c^2}{8\pi D^2 X} I_1\left(\frac{cX}{2D}\right)\exp\left(-c^2 t/2D\right), \qquad X \equiv \left(c^2t^2 - r^2\right)^{1/2} > 0 \tag{43}$$

where $I_1(x)$ is the modified Bessel function. (Morse and Feshbach use a different normalization. To normalize so that the integral over all space is unity, their solution must be multiplied by $1/4\pi D$).

The most complete theoretical treatment of photon transport is the Elastic Boltzmann Transport Equation. Detailed solutions to this equation have been obtained by Cai, Alfano, et al. [21].

8.6 SUMMARY AND COMPARISON WITH MONTE CARLO MODEL

To summarize: based on the diffusion equation for isotropic scattering, in a uniform scattering medium for an impulse of photon emission at $t = 0$, $r = 0$, at a given range r, for long times the density decays as $t^{-3/2}$, the total photon exit rate through a sphere decays as $t^{-5/2}$, and the first-passage exit rate through a sphere decays as $\exp(-D\pi^2 t/R^2) = \exp(-\pi^2 cLt/(3R^2)) = \exp(-\pi^2 ct/(3R(R/L))$. Figure 18 compares the probability density of first-passage time from diffusion theory (solid lines) and from the results of the Monte Carlo model (circles). The abscissa indicates the time after the laser pulse strikes the target. Note changes in scales from graph to graph. We again assume that R = 100 m. The vertical dashed line indicates the ballistic photon flight time = R/c = 0.33 μsec.

The figure shows that the results from the two theories converge as R/L increases and as g decreases, which is expected. We conclude that the Monte Carlo model is consistent with diffusion theory. For the very early-arriving photons analyzed in Section 6, the model applies but the diffusion equation does not.

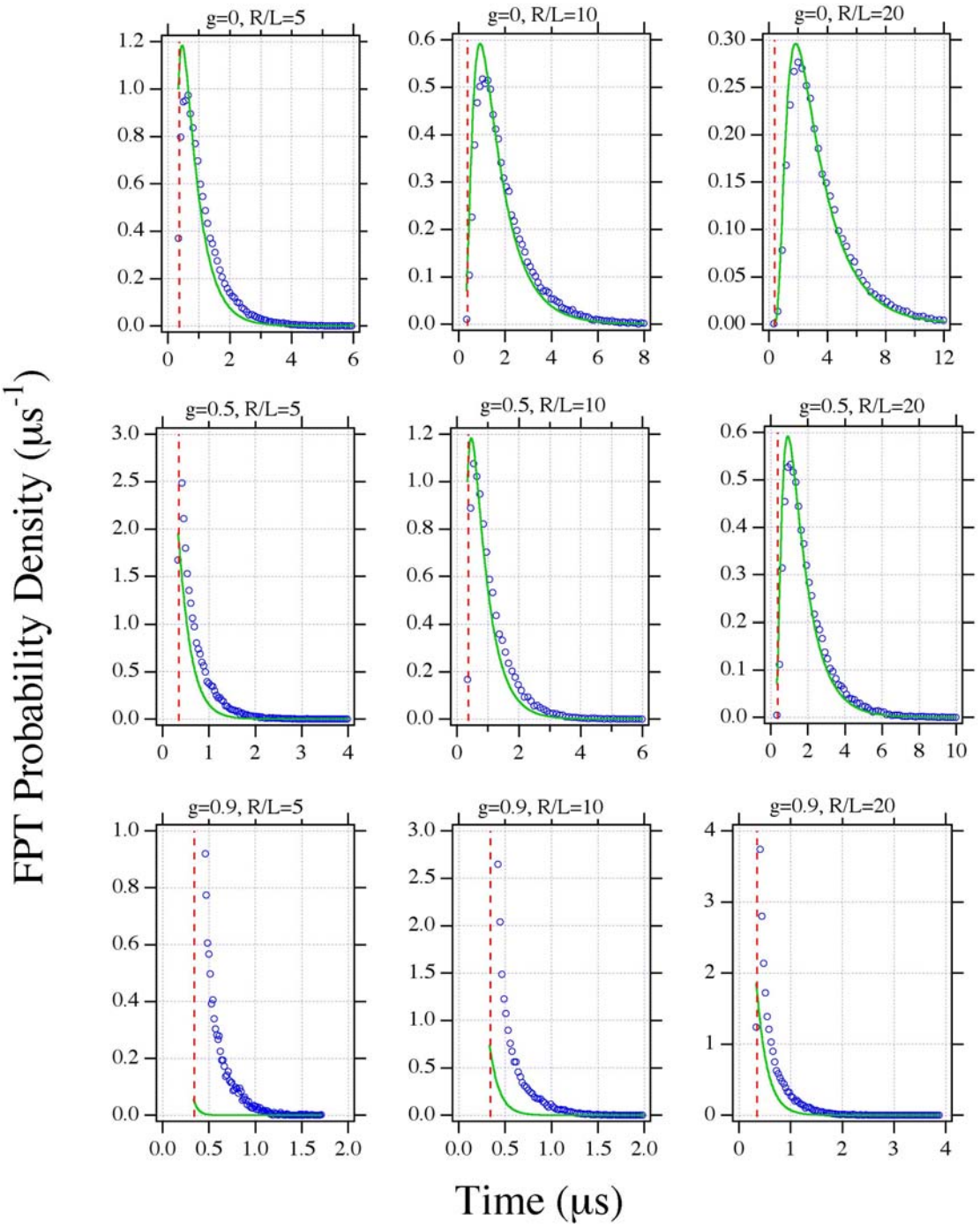

Figure 18. Comparison of Results from Diffusion Theory and from Monte Carlo Model

9. CONCLUSION

The IDA Flash Lidar Monte Carlo model can provide a useful tool for estimating the quality of 3D imagery from flash lidar through obscurants and for sorting out the effects of ballistic, diffuse, and "noise" photons. In principle, moving targets could be imaged if the sensor/processor could track the target, estimate its 3D translation and rotation as a function of time, and place photons in the correct voxels accordingly. The Geiger Remapping Technique can be a useful tool for interpreting images made using Geiger detectors.

APPENDIX A: METHOD OF GENERATING RANDOM SCATTERING ANGLES ACCORDING TO THE SINE–WEIGHTED HENYEY–GREENSTEIN DISTRIBUTION [7]

For Monte Carlo simulations it is necessary to select θ-values from the sine-weighted Henyey-Greenstein (HG) function, given by

$$W(\theta) = \tfrac{1}{2}\sin\theta\,\Phi(\theta) = \frac{\sin\theta(1-g^2)}{2\left(1+g^2-2g\cos\theta\right)^{3/2}} \quad . \tag{A1}$$

Here, the solid-angle factor of $\sin\theta$ is included directly in the probability density function (cf. Eq. 2) and the normalization condition is

$$\int_0^{2\pi} d\phi \int_0^{\pi} W(\theta)\,d\theta = 2\pi \int_0^{\pi} \frac{\sin\theta(1-g^2)\,d\theta}{2\left(1+g^2-2g\cos\theta\right)^{3/2}} = 1 \quad . \tag{A2}$$

(The $g = 0$ case, namely isotropic scattering, is easily checked.)

We now wish to generate random values of θ with probability density given by (A1). A general method for generating random numbers with a specified density is outlined in [8], Chapter 7. Let x be uniform in [0, 1]; that is, x has density function

$$\rho(x) = \begin{cases} 1; & 0 \le x \le 1 \\ 0; & \text{otherwise} \end{cases} \quad . \tag{A3}$$

Assume there is a function $\theta = f(x)$ that transforms ρ into W. By conservation of probability, W must satisfy

$$\left|\rho(x)\,dx\right| = \left|W(\theta)\,d\theta\right| \quad . \tag{A4}$$

Rearranging, one finds

$$\frac{dx}{d\theta} = W(\theta) \quad , \tag{A5}$$

which is easily integrated to yield

$$x = \int W(\theta)\,d\theta = F(\theta) \quad . \tag{A6}$$

Here $F(\theta)$ is the cumulative distribution. The desired transformation is given by the inverse of the cumulative distribution function, namely

$$\theta = f(x) = F^{-1}(x) \tag{A7}$$

In order to arrive at a closed-form solution for *f*, we require both a closed-form expression for the cumulative distribution, and a closed-form expression for the inverse. For the sine-weighted HG function, both closed-form expressions exist.

Using equation-solving software, the cumulative probability function is found by computing the integral

$$F(\theta) = \int_0^\theta \frac{\sin\xi\,(1-g^2)\,d\xi}{2\left(1+g^2-2g\cos\xi\right)^{3/2}} = \frac{(1-g^2)}{2g}\left(\frac{1}{1-g} - \frac{1}{\sqrt{1+g^2-2g\cos\theta}}\right) \quad , \tag{A8}$$

and the inverse function is found to be

$$\theta = f(x) = F^{-1}(x) = \cos^{-1}\left(\frac{1-2x+2g(1-x+x^2)+g^2(1-2x)+2g^3x(x-1)}{(2gx-1-g)^2}\right) \quad . \tag{A9}$$

APPENDIX B: MODEL OF ALCOCK AND HATCHETT—SMALL–ANGLE SCATTERING

Using the equations of radiative transport in a scattering medium and under the assumption of very small scattering angles, Alcock and Hatchett [19] computed an exact solution for photon scattering vs. angle and time. Their results have been frequently quoted and used, for example, in [22]. A brief summary of their results follows.

In the notation of [19], ϕ = angle between photon trajectory and radius vector, θ = scattering angle, κ = scattering coefficient = $1/L$, τ = optical depth = R/L, N = total photon number, $\gamma = ct/L$, and $\zeta = \phi^2$. Alcock and Hatchett obtain an expression for the intensity (m^{-2} s^{-1}), given by

$$I(\phi,t) = \frac{N\kappa c}{4\pi^2 R^2} P(\varsigma,\gamma;\tau) \quad . \tag{B1}$$

In the limit of $\tau \to \infty$, that is, a large number of scatterings they show that

$$P(\zeta,\gamma;\tau) = \frac{1}{<\theta^2>^2 \tau^3} G\left(\frac{\zeta}{\tau <\theta^2>}, \frac{\gamma}{\tau^2 <\theta^2>}\right) \quad , \tag{B2}$$

where G is a complicated integral function given, and graphed, in [19]. The integral over angle is

$$P(\gamma;\tau) = \frac{4\pi^2}{\tau^2 <\theta^2>} \sum_{n=1}^{\infty} (-1)^{n+1} n^2 \exp\left(\frac{-2n^2\pi^2\gamma}{\tau^2 <\theta^2>}\right) \quad . \tag{B3}$$

In our notation, the intensity (m^{-2} s^{-1}) vs. time is found from (B1) and (B3) to be

$$I(t) = \frac{NcL}{R^4 <\theta^2>} \sum_{n=1}^{\infty} (-1)^{n+1} n^2 \exp\left[-\left(\frac{n\pi}{R}\right)^2 \frac{2cLt}{<\theta^2>}\right] \quad . \tag{B4}$$

By comparison, our (43) is

$$I(t) = \frac{N\pi cL}{3R^4 <\theta^2>} \sum_{n=1}^{\infty} (-1)^{n+1} n^2 \exp\left[-\left(\frac{n\pi}{R}\right)^2 \frac{2cLt}{3<\theta^2>}\right] \quad . \tag{B5}$$

The coefficient of (B5) is $\pi/3$ times that of (B4); more importantly, the exponent of (B5) is 1/3 that of (B4). These differences are discussed in Appendix C.

APPENDIX C: DIFFUSION CONSTANT

This Appendix documents the construction of appropriate rotation matrices with which to implement the random walk for the Ballistic Imaging model. In the limit of a large number of scattering events the random walk can be treated as an isotropic diffusion problem; the diffusion constant for this limit is derived

By convention, the photon travel direction is chosen to be along the positive *z* axis of the current frame (the "photon frame"). That is, in the current photon frame the direction of travel is always (0,0,1). The net photon displacement must be computed in a global coordinate system ("lab frame"). The transformation from photon frame to lab frame is accomplished by a suitable product of rotation matrices, developed below.

Each scattering event is described by two angles, θ and ϕ. The polar angle θ is measured from the positive *z* axis of the frame before scattering to the positive *z* axis of the frame after scattering, and is chosen from the sine-weighted Henyey Greenstein probability density. The azimuthal angle ϕ is measured from the positive *x* axis of the frame before scattering to the positive *x* axis of the frame after scattering, and is chosen from a uniform probability density on [0, 2π). The path length between two scattering events is selected from an exponential probability density

$$f(l) = \tfrac{1}{L} e^{-l/L} \quad , \tag{C1}$$

where L is the mean free path.

Figure C-1 shows the relation between the frames before and after a scattering event. The (x, y, z) frame is before scattering, while the (x'',y'',z'') frame is after scattering. The rotation order convention is to rotate first by ϕ about the *z* axis to yield the (x', y', z') frame, then by θ about the x' axis to give the (x'', y'', z'') frame. The net rotation is built up in two steps. The coordinates of a vector in the (x', y', z') frame are expressed in terms of the coordinates in the (x, y, z) frame through

$$\begin{pmatrix} x \\ y \\ z \end{pmatrix} = \begin{pmatrix} \cos\phi & -\sin\phi & 0 \\ \sin\phi & \cos\phi & 0 \\ 0 & 0 & 1 \end{pmatrix} \begin{pmatrix} x' \\ y' \\ z' \end{pmatrix} = R_z(\phi) \begin{pmatrix} x' \\ y' \\ z' \end{pmatrix} \quad . \tag{C2}$$

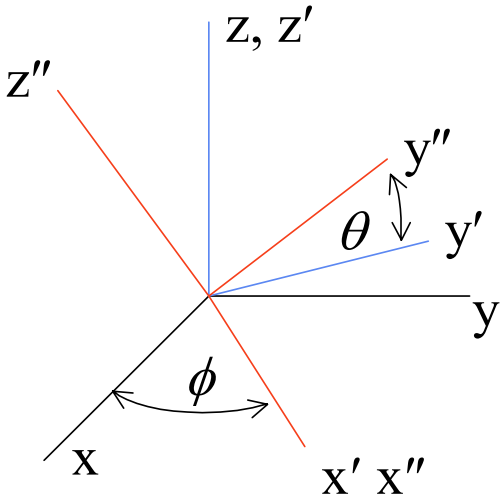

Figure C-1. Coordinate Systems

Similarly, the coordinates of a vector in the (x', y', z') frame are expressed in terms of the coordinates in the (x'', y'', z'') frame through

$$\begin{pmatrix} x' \\ y' \\ z' \end{pmatrix} = \begin{pmatrix} 1 & 0 & 0 \\ 0 & \cos\theta & -\sin\theta \\ 0 & \sin\theta & \cos\theta \end{pmatrix} \begin{pmatrix} x'' \\ y'' \\ z'' \end{pmatrix} = R_x(\theta) \begin{pmatrix} x'' \\ y'' \\ z'' \end{pmatrix} \quad . \tag{C3}$$

The net rotation relating coordinates before and after scattering is

$$\begin{pmatrix} x \\ y \\ z \end{pmatrix} = R_z(\phi)R_x(\theta) \begin{pmatrix} x'' \\ y'' \\ z'' \end{pmatrix} = \begin{pmatrix} \cos\phi & -\sin\phi\cos\theta & \sin\phi\sin\theta \\ \sin\phi & \cos\phi\cos\theta & -\cos\phi\sin\theta \\ 0 & \sin\theta & \cos\theta \end{pmatrix} = M(\phi,\theta) \begin{pmatrix} x'' \\ y'' \\ z'' \end{pmatrix} \quad . \tag{C4}$$

The n^{th} scattering event is described by the rotation matrix $M_n = M(\phi_n, \theta_n)$. Since the photon direction is always (0,0,1) in the current photon frame, the photon direction in the lab frame is found by transforming (0,0,1) *backwards n* times via the matrix product

$$\mathbf{v_n} = M_1 M_2 \ldots M_n \begin{pmatrix} 0 \\ 0 \\ 1 \end{pmatrix} \quad . \tag{C5}$$

Letting S_n denote the matrix product at the nth scattering event, and $\mathbf{k}$ denote (0,0,1) in the current photon frame, one then arrives at the "scattering direction map" given by

$$\begin{aligned} \mathbf{v_n} &= S_n \mathbf{k} \\ S_{n+1} &= S_n M_{n+1} \;\; ; \;\; S_0 = 1 \end{aligned} \quad . \tag{C6}$$

In the lab frame the net displacement of the photon after n steps is

$$\mathbf{R}_n = \sum_{\alpha=1}^{n} \mathbf{r}_\alpha = \sum_{\alpha=1}^{n} l_\alpha \mathbf{v}_\alpha = \sum_{\alpha=1}^{n} l_\alpha S_\alpha \mathbf{k} \quad , \tag{C7}$$

where l_α is the step length at step α.

The diffusion constant for the random walk is found as follows. The mean square displacement after n steps is

$$< R_n^{\,2} > = < \mathbf{R}_n^{\,T} \mathbf{R}_n > = \left\langle \left(\sum_{\alpha=1}^{n} l_\alpha S_\alpha \mathbf{k} \right)^T \left(\sum_{\beta=1}^{n} l_\beta S_\beta \mathbf{k} \right) \right\rangle \quad , \tag{C8}$$

where T denotes the transpose operation and <> denotes ensemble average. Simple manipulation yields

$$< R_n^{\,2} > = \sum_{\alpha=1}^{n} < l_\alpha^{\,2} \mathbf{k}^T S_\alpha^{\,T} S_\alpha \mathbf{k} > \; + 2 \sum_{\alpha=1}^{n-1} \sum_{\beta=\alpha+1}^{n} < l_\alpha \, l_\beta \, \mathbf{k}^T S_\alpha^{\,T} S_\beta \mathbf{k} > \quad . \tag{C9}$$

The first sum (diagonal terms) evaluates to $n <l^2>$, since the S_α are orthogonal matrices and satisfy $S_\alpha^{\,T} = S_\alpha^{\,-1}$. In the second sum (off diagonal terms) the average over step lengths and angles factors, since the step lengths and the scattering angles come from statistically independent physical processes. Also, the steps lengths are independent, so $<l_\alpha \, l_\beta> = <l_\alpha><l_\beta> = <l>^2$. Applying these facts to (C9) yields

$$< R_n^{\,2} > = n < l^2 > \; + 2 < l >^2 \sum_{\beta>\alpha} \mathbf{k}^T < S_\alpha^{\,T} S_\beta > \mathbf{k} \quad . \tag{C10}$$

The average in the sum is given by

$$\begin{aligned} < S_\alpha^{\,T} S_\beta > &= < (M_1 M_2 \ldots M_\alpha)^T (M_1 M_2 \ldots M_\beta) > \\ &= < M_\alpha^{\,T} M_{\alpha-1}^{\,T} \ldots M_1^{\,T} M_1 M_2 \ldots M_\beta > \\ &= < M_{\alpha+1} M_{\alpha+2} \ldots M_\beta > \\ &= < M >^{\beta-\alpha} \end{aligned} \quad , \tag{C11}$$

where the third equality follows from orthogonality and the last equality follows from the independence of the scattering events. Using the fact that $<\sin\phi> = <\cos\phi> = 0$ the average rotation matrix is found from (C4) to be

$$< M > = \begin{pmatrix} 0 & 0 & 0 \\ 0 & 0 & 0 \\ 0 & < \sin\theta > & < \cos\theta > \end{pmatrix} \quad . \tag{C12}$$

Therefore

$$< M >^k = \begin{pmatrix} 0 & 0 & 0 \\ 0 & 0 & 0 \\ 0 & < \cos\theta >^{k-1} < \sin\theta > & < \cos\theta >^k \end{pmatrix} \quad , \tag{C13}$$

and it follows that

$$< R_n^{\,2} > = n < l^2 > \; + 2 < l >^2 \sum_{\alpha=1}^{n-1} \sum_{\beta=\alpha+1}^{n} < \cos\theta >^{\beta-\alpha} \quad . \tag{C14}$$

The double sum can be evaluated by recognizing there are (n-k) terms of $<\cos\theta>^k$, hence

$$\sum_{\alpha=1}^{n-1} \sum_{\beta=\alpha+1}^{n} < \cos\theta >^{\beta-\alpha} = \sum_{k=1}^{n-1} (n-k) < \cos\theta >^k \quad . \tag{C15}$$

The second sum in (C15) can be evaluated by standard techniques[1] and the result is

$$\sum_{k=1}^{n-1} (n-k) < \cos\theta >^k = \frac{< \cos\theta >^{n+1} - n < \cos\theta >^2 + (n-1) < \cos\theta >}{(1 - < \cos\theta >)^2} \quad . \tag{C16}$$

Since the steps are chosen from an exponential probability density the mean square step length and mean free path are related via[2] $< l^2 > = 2 < l >^2 = 2L^2$. The mean square displacement is then

$$< R_n^{\,2} > = < l^2 > \left(n + \frac{< \cos\theta > \left(< \cos\theta >^n - n < \cos\theta > + n - 1 \right)}{(1 - < \cos\theta >)^2} \right) \quad . \tag{C17}$$

For large n and for sufficiently large scattering angles θ (to be discussed further below), $< \cos\theta >^n$ can be neglected in the numerator of (C17) and one arrives at

$$< R_n^{\,2} > \sim \frac{n < l^2 >}{1 - < \cos\theta >} \quad . \tag{C18}$$

For a three-dimensional random walk the diffusion constant is related to the mean square displacement and the flight time through [23]

---

1 First rewrite the sum as $\sum_{j=1}^{n-1} j < \cos\theta >^{n-j} = \frac{1}{q^n} \sum_{j=1}^{n-1} j\, q^j = \frac{1}{q^{n-1}} \frac{\partial}{\partial q} \left(\sum_{j=1}^{n-1} q^j \right)$, where $q = (<\cos\theta>)^{-1}$. The sum inside parenthesis is a geometric sum that evaluates to $\frac{q - q^n}{1 - q}$. Carrying out the necessary operations yields the expression in (C16).

2 The mean square step length is given by $< l^2 > = \int_0^\infty l^2\, \rho(l)\, dl = \frac{1}{L} \int_0^\infty l^2\, e^{-l/L}\, dl = 2L^2$.

$$< R^2 >= 6Dt \quad . \tag{C19}$$

Combining (C18) and (C19) and using the fact that after n scatterings the average path length is $nL=ct$, where c is the speed of light and that $< l^2 >= 2L^2$, the diffusion constant is given by

$$D = \frac{cL}{3(1- < \cos\theta >)} \quad . \tag{C20}$$

We now examine the restriction on the scattering angle θ in arriving at the approximation in (C18). The approximation starts with

$$< \cos\theta >^n << n1\left(- < \cos\theta >\right) \quad , \tag{C21}$$

which for small angles becomes

$$\begin{aligned} & < 1 - \tfrac{\theta^2}{2} >^n << n\left(1- < \tfrac{\theta^2}{2} >\right) \\ & 1 - \tfrac{n}{2} < \theta^2 > << \tfrac{n}{2} < \theta^2 > \\ & n < \theta^2 > \; >> 1 \end{aligned} \quad , \tag{C22}$$

or

$$\sqrt{n}\theta_{rms} >> 1 \quad . \tag{C23}$$

The central assumption in Alcock and Hatchett's treatment [19] of X-ray scattering is that of extremely small scattering angles and a relatively small number of scattering events, characterized by the opposite condition to (C23), namely [24]

$$\sqrt{n}\theta_{rms} << 1 \quad . \tag{C24}$$

The diffusion analysis outlined in this Appendix does not, therefore, apply to their treatment. In fact, Alcock and Hatchett say (pp. 459–460), "These formulae are all developed under the assumption that the resultant angle of the photon trajectory after any number of scatterings is small. This requirement keeps the analysis in a quantitatively different regime from that of random walk analyses, and the results are qualitatively different."

REFERENCES

[1] Sears, S. W., *Thermodynamics*, New York: Addison-Wesley, 1953

[2] Accetta, J., and D. L. Schumaker, *The Infrared and Electro-Optical Systems Handbook*, Ann Arbor, MI: Environmental Research Institute of Michigan (ERIM), 1993

[3] Wang, L., P. Ho, C. Liu, G. Zhang, and R. Alfano, "Ballistic 2D Imaging Through Scattering Walls Using an Ultrafast Optical Kerr Gate," *Science*, Vol. 253, pp. 769-771, 16 August 1991

[4] DOD-HDBK-178(ER), "Quantitative Description of Obscuration Factors for Electro-Optical and Millimeter-Wave Systems," U. S. Army, 1986

[5] Peng, Q., R. T. Snider, T. E. Cowan, S. M. Herman, M. D. Perry, and D. P. Schissel, "Lidar Cloud Penetration Simulator," Proceedings of the 2001 AMOS Conference, Wailea, Maui, pp. 492 – 499.

[6] Van de Hulst, H. C., *Multiple Light Scattering: Tables, Formulas, and Applications*, New York: Academic Press, 1980

[7] Sullivan, R., et al., "Ballistic Imaging Lidar," Proceedings of the 2001 AMOS Conference, Wailea, Maui, pp. 636 -- 641.

[8] Press, W. H., et al., *Numerical Recipes: The Art of Scientific Computing*, Cambridge: University Press, 1986

[9] Hernandez, J. J. et al., "Probability, Statistics, and Monte Carlo," in "Review of Particle Properties," *Physics Letters B*, Vol. 239, pp. III-28 to III-38 (12 April 1990)

[10] Jackson, J. D., *Classical Electrodynamics*, 2nd Ed., Wiley 1975

[11] Allen, C. W., *Astrophysical Quantities*, 2nd Edition, London: The Athlone Press, 1963.

[12] Ludwig, D. *et al*., "Identifying Targets under Trees – Jigsaw 3D-LADAR Test Results," Proceedings of SPIE Vol. 5086, 2003

[13] Aull, B. F. *et al.*, "Geiger-Mode Avalanche Photodiodes for Three-Dimensional Imaging," MIT Lincoln Laboratory Journal, Vol. 13, Number 2, p. 335, 2002

[14] Albota, M. A. *et al.*, "Three-Dimensional Imaging Laser Radars with Geiger-Mode Avalanche Photodiode Arrays," MIT Lincoln Laboratory Journal, Vol. 13, Number 2, p. 351, 2002

[15] Crank, J., *The Mathematics of Diffusion*, New York: Oxford University Press, 1975

[16] Morse, P. M. and Feshbach, H., *Methods of Theoretical Physics*, New York: McGraw Hill, 1953

[17] Hughes, Barry D., *Random Walks and Random Environments, Vol. 1: Random Walks*, Oxford: Clarendon Press, 1995.

[18] Askebjer, P., et al. (36 authors), "Optical Properties of Deep Ice at the South Pole: Absorption," *Applied Optics*, Vol. 36, No. 18, p. 4168, 1997

[19] Alcock, C., and S. Hatchett, "Effects of Small-Angle Scattering on a Pulse of Radiation with an Application of X-ray Bursts and Interstellar Dust," Astrophysical Journal, Vol. 222, pp. 456 – 470, 1978.

[20] Zwillinger, D. (Ed.). CRC Standard Mathematical Tables and Formulae, Boca Raton, FL: CRC Press, p. 417, 1995

[21] Cai, W., M. Lax, and R. Alfano, "Analytical Solution of the Elastic Boltzmann Transport Equation in an Infinite Uniform Medium Using Cumulant Expansion," J. Physical Chemistry, Vol. 104, No. 16, pp. 3996-4000, 2000.

[22] Miralda-Escude, J., "Small-Angle Scattering of X-rays from Extragalactic Sources by Dust in Intervening Galaxies," Astrophysical Journal, Vol. 512, pp. 21–24, 1999.

[23] Chandrasekhar, S., "Stochastic Problems in Physics and Astronomy," Rev. Mod. Phys., Vol. 15, pp. 1-89, 1943.

[24] Hatchett, S., private communication, March 2003.

REPORT DOCUMENTATION PAGE

Form Approved
OMB No. 0704-0188

1. REPORT DATE	2. REPORT TYPE	3. DATES COVERED *(From–To)*
March 2004	Final	September 2001–August 2002

4. TITLE AND SUBTITLE

Flash Lidar: Monte Carlo Estimates of Ballistic, Diffuse, and Noise Photons as Recorded by Linear and Geiger Detector Arrays

5a. CONTRACT NUMBER
DAS W01 98 C 0067/DAS W01 04 C 0003

5b. GRANT NUMBER

5c. PROGRAM ELEMENT NUMBER

6. AUTHOR(S)

R. Sullivan, J. Franklin, J. Heagy

5d. PROJECT NUMBER

5e. TASK NUMBER
CRP-2075

5f. WORK UNIT NUMBER

7. PERFORMING ORGANIZATION NAME(S) AND ADDRESS(ES)

Institute for Defense Analyses
4850 Mark Center Drive
Alexandria, VA 22311-1882

8. PERFORMING ORGANIZATION REPORT NUMBER

IDA Paper P-3833

9. SPONSORING / MONITORING AGENCY NAME(S) AND ADDRESS(ES)

DARPA/TTO
3701 N. Fairfax Drive
Arlington, VA 22203

10. SPONSOR/MONITOR'S ACRONYM(S)

11. SPONSOR/MONITOR'S REPORT NUMBER(S)

12. DISTRIBUTION / AVAILABILITY STATEMENT

Approved for public release, distribution unlimited. (11 August 2004)

13. SUPPLEMENTARY NOTES

14. ABSTRACT

A description is provided of a model that estimates the numbers of ballistic photons, diffuse photons, and "noise photons" arriving at the focal plane array of a lidar, resulting from a series of pulses of laser energy directed at a target, in the presence of obscurant. Inputs to the model include laser wavelength, pulse energy, number of pulses integrated, obscurant optical depth (number of scattering lengths) and forward scattering factor, target range, target structure and reflectivity, lidar aperture diameter and focal length, pixel pitch, time bin, detector noise level, and an efficiency factor related to such parameters as optics transmissivity, beam-spreading factor, detector fill factor, and detector quantum efficiency. Model outputs include three-dimensional plots of numbers of ballistic, diffuse, and noise photons versus focal plane array (FPA) x and y coordinate, and time delay after first ballistic photon arrival, for both linear and Geiger-mode detector arrays. The model can be useful for performance prediction of flash lidars in the presence of obscurants. A procedure is provided for remapping Geiger images, to improve their interpretability. The model is also shown to agree with diffusion theory in the limit of large optical depth and small forward scattering factor.

15. SUBJECT TERMS
lidar, ladar, laser radar, 3D imaging, ballistic imaging

16. SECURITY CLASSIFICATION OF:			17. LIMITATION OF ABSTRACT	18. NUMBER OF PAGES	19a. NAME OF RESPONSIBLE PERSON
					Dr. Tim Grayson
a. REPORT Uncl.	b. ABSTRACT Uncl.	c. THIS PAGE Uncl.	U/L	58	19b. TELEPHONE NUMBER *(include area code)* 703-696-2230